ABSTRACT

Title of Dissertation:	MICROSYSTEM TECHNOLOGIES FOR AIRBORNE VIRUS QUANTIFICATION
	Siddharth Raghu Srimathi, Doctor of Philosophy, 2025
Dissertation directed by:	Professor Don L. DeVoe, Department of Mechanical Engineering

Advancing our ability to measure and characterize viruses is essential for progress in clinical diagnostics, vaccine development, and understanding airborne transmission in infectious disease research. However, existing assays often involve long turnaround times, high costs, and labor-intensive procedures. This dissertation presents two complementary microfluidic platforms developed to address these challenges: a digital focus assay (dFA) for viable viral quantification and a droplet merging platform for the compositional analysis of bioaerosols.

The dFA employs an array of independent nanoliter cell cultures, with cells in each microwell inoculated with virus and isolated by oil discretization to prevent cross-contamination. Following incubation, infected cells are detected by immunofluorescent staining, and automated image analysis generates a binary map of wells positive for viral antigen. Statistical analysis of these data yields infectious viral titers using

significantly smaller sample and reagent volumes than conventional focus assays, while enhancing assay automation and endpoint time flexibility. Demonstrated with both model virus and clinical influenza A specimens, the platform provides an accurate, rapid, cost-effective, and convenient tool for viral load quantification with broad clinical, pharmaceutical, and research applications.

The droplet merging platform addresses fundamental questions in aerovirology, such as the distribution of virus within aerosol droplets and the quanta of infection. Approaches for collecting aerosols as discrete aqueous droplets in oil are explored, along with model emulsions generated using a microfluidic droplet generator. Controlled merging of individual or small numbers of droplets with assay reagents is demonstrated, which provides a framework for compositional analysis at the single-particle level. Proof-of-concept assays are explored for viral protein detection, along with an assessment of potential limitations. Finally, integration of the droplet merging platform with the dFA is discussed as a strategy for quantifying viable viruses in aerosols, offering new tools to investigate key open questions in aerovirology.

MICROSYSTEM TECHNOLOGIES FOR AIRBORNE VIRUS QUANTIFICATION

by

Siddharth Raghu Srimathi

Dissertation submitted to the Faculty of the Graduate School of the
University of Maryland, College Park, in partial fulfillment
of the requirements for the degree of
Doctor of Philosophy
2025

Advisory Committee:
Professor Don L. DeVoe, Chair
Associate Professor Margaret A. Scull, Co-Chair
Professor Donald K. Milton
Professor Srinivasa R. Raghavan
Associate Professor Ganesh Sriram

© Copyright by
Siddharth Raghu Srimathi
2025

Dedication

To my parents, whose commitment and sacrifice made this journey possible. To Indu, for inspiring me and showing me a path forward. To Bhuvsmita, whose love and support made this chapter joyful.

Acknowledgements

I am sincerely thankful to my advisor, Dr. Don DeVoe, for his constant encouragement and trust throughout my Ph.D. His guidance allowed me the independence to work on my dissertation while also exploring other research directions. He has always backed my ideas and recognized my achievements. This mentorship has been instrumental in helping me grow as a researcher and work toward my professional goals. I could not have asked for a better advisor.

I am also thankful to Dr. Jung Yeon Han and Dr. Jaesung Lee for welcoming me into the group and being outstanding mentors, from helping me navigate the challenging early days of graduate school to guiding my research and professional development. I am grateful to Michael Yeh, whose training in the early days laid the foundation for my proficiency and growth in microfabrication.

I extend my thanks to my co-advisor, Dr. Margaret Scull, for welcoming me into her group, guiding me, and encouraging me to explore the unfamiliar waters of biology as an engineer with no prior background. I am grateful to Maxinne Ignacio and Maria Corkran for teaching me the practical skills of cell culture, virology, and immunostaining, which enabled me to become self-sufficient in the biological aspects of my research.

I would also like to thank Dr. Sheldon Tai for always being supportive, resourceful, and accommodating whenever I needed to run an assay. I am thankful to Dr. Proma Bhattacharya for her kindness in helping me and collaborating on my independent research ventures.

I sincerely thank my committee members, Dr. Akua Asa-Awuku, Dr. Don Milton, Dr. Srinivasa Raghavan, and Dr. Ganesh Sriram, for their time, guidance, and insightful feedback on my research.

I am also grateful to the Fablab staff at the UMD Nanocenter: Dr. Kim, Tom, Mark, and Jon, for training me and offering a helping hand whenever I needed it.

Finally, I am grateful to all the members of MML: Michael, Supriya, Han, Jaesung, Proma, Sima, Kat, and Ethan, for being the best lab mates I could ask for and for making my time here a pleasure.

Table of Contents

Dedication ii
Acknowledgements iii
Table of Contents v
List of Figures vii
Chapter 1: Background 1
Motivation 1
Aerosol Sampling Methods for Studying Viral Distribution and Viability 5
Microfluidic emulsion generation for viral aerosol modeling 9
Chapter 2: Microfluidic digital focus assays for the quantification of infectious influenza virus 13
Experimental 15
Device Design and Fabrication 15
Cell Seeding 20
Virus Inoculation and Well Discretization 21
Fixing and Staining 22
Clinical Specimen Analysis 23
Results 24
Efficient discretization and uniform flow are enabled by the dFA chip design 24
MDCK cells form confluent, isolated monolayers within the dFA platform 27
Infectious influenza A virus titers can be determined using the dFA platform 30
The dFA platform is compatible with clinical specimens 37
Discussion 38
Acknowledgements 45
Chapter 3: Microfluidic discretization for single-particle analysis of aerosol emulsions 46
Experimental 47
Aerosol collection as emulsions using CGT 47
Microfluidic droplet generation 48
Droplet merging in microwell arrays 52
Demonstration of the droplet merging technology using a bead-based sandwich assay 56
Results 61
Collection of aerosols as emulsions using CGT 61
Distribution of the sedimented droplets over discretized microwells 62
Droplet merging 63
Discussion 64
Aerosol collection as emulsion 64
Droplet merging issues 66
Issues with the sandwich assay 67
Acknowledgements 69
Chapter 4: Conclusion and Future Directions 71
Conclusions 71
Future directions 72

Improvements to the dFA platform 72
Improvements to the Droplet Merging Platform 75
Improvements to Magnetic Bead-Based Assay 76
Combining the dFA platform with droplet merging 77
Concluding Remarks and Perspectives 78
List of Publications and Conference Presentations 90
Publications that have appeared in print: 90
Presentations that have been delivered: 90

List of Figures

Figure 1.1. (A) The BioSpot VIVAS, a condensation growth tube (CGT)-based aerosol sampler developed by Aerosol Devices and used in this dissertation for aerosol sampling experiments. (B) The BioSpot VIVAS with the front door open, showing the condensation growth tube and the temperature-controlled zones of the wetted wall column. 9
Figure 2.1. Conceptual comparison of conventional and digital focus assays for infectious virus quantification. (A) In a conventional FFA, assay readout is performed in a narrow time window following primary infection but before excessive replication can occur to ensure the growth of small discrete foci for quantification. (B) The digital focus assay sequesters virus within a large number of discrete microwells, enabling binary readout from individual wells after extended replication with indirect quantification based on statistical analysis. 14
Figure 2.2. Fabrication schematics of the SU-8 master mold and the PDMS microfluidic device. (A) 120 μm SU-8 2075 is coated on a 4" Si wafer and patterned through photolithography (B) After a short post-exposure bake, a second layer of SU-8 was coated on top and patterned through photolithography (C) The unexposed SU-8 was developed away completing the fabrication of the mold (D) 10:1 PDMS was poured over the SU-8 mold and cured at 80 °C for 3 hours (E) The cured PDMS was cut and bonded to a 3" glass slide through oxygen plasma activation (F) An unpatterned PDMS block with holes punched for inlet and outlet ports was bonded over the patterned microwell PDMS layer, completing the PDMS device fabrication ... 15
Figure 2.3. Overview of the dFA chip geometry. (A) Cross-sectional schematic of a PDMS chip bonded to the glass slide, with feature dimensions indicated. (B) Perspective view of a chip revealing the 13x13 microwell array and enclosing channel with inlet and outlet pillar arrays designed for improved cell seeding uniformity. (C) Image of a fabricated multi-layer SU-8 patterned wafer with 8 devices per mold. D) An image of the enclosed PDMS microwell array chip. Scale bar: 4 mm. 17
Figure 2.4. Hydrophilic surface modification through embedded Pluronic surfactant. (A) Pluronic F-108 embedded into the PDMS matrix yields a hydrophilic surface after overnight exposure to water. (B) Cross-sectional schematic and image of the 200 μm PDMS microwells without embedded Pluronic F-108. Flowing mineral oil over the microwells prefilled with water caused dewetting and partial ejection of water from the microwells. (C) Cross-sectional schematic and image of the 200 μm PDMS microwells with embedded Pluronic F-108. Flowing mineral oil over the microwells yields perfect discretization of the microwells without observable loss of water. Scale bar: 500 μm. 18
Figure 2.5. Digital focus assay process. (A) As MDCK cell suspension flows into the chip, the cells sediment into the microwells and adhere to the walls after incubation at 37 °C with 5% CO_2. (B) Overnight incubation resulted in nearly confluent MDCK cell growth within individual microwells. (C) Influenza A virus inoculum is introduced into the chip and incubated for 2 h. (D) Overlay medium is introduced into the chip that flushed out any unadsorbed virus from the chip. (E) Mineral oil is introduced into the chip to discretize the microwells and prevent cross-contamination between their volumes. (F) Discretized microwell arrays containing the cultured MDCK cells inoculated with influenza A virus and filled with an overlay medium are incubated for 22 h. (G-I) The oil and overlay media are flushed out with PBS at the end of the assay to permit fixing, permeabilization, and immunofluorescent staining of the cells. 19

Figure 2.6. Images showing the MDCK cell culture progression from 0-24 hours within PDMS microwells 20
Figure 2.7. Cell suspension flow simulation results. COMSOL Multiphysics simulation depicting the flow behavior of cell suspension liquids through (A) a rectangular enclosing channel without pillar arrays, (B) a rectangular enclosing channel with pillar arrays on the inlet, (C) a rectangular enclosing channel with pillar arrays on both the inlet and the outlet, and (D) a continuously curving channel with pillar arrays on both the inlet and the outlet, designed to promote mixing and uniform lateral distribution of the cells to the microwell arrays. Scale bar: 3 mm. 26
Figure 2.8. Distribution of MDCK cells. (A) Sample image displaying typical MDCK cell distribution across the 13x13 microwell array following cell seeding, expansion, and nuclear staining for visualization. Scale bar: 500 µm. (B) Distributions of cells within 9 individual chips. (C) Mean and (D) standard deviation for aggregate cell distributions within each array position across all 9 chips used for the digital focus assay with MM overlay. 28
Figure 2.9. Impact of overlay medium on cell bridging across microwells. Quantification of cell bridging events between adjacent microwells for MCC and MM overlays at 8 h and 24 h time points. Bridging probability is defined as number of bridging events observed scaled by the total number of adjacent well gaps across which bridging may occur within a single array (n=10 chips for each overlay). Insets of high and low bridging example cases are included. 30
Figure 2.10. Digital assay readout. (A) Paired images of Influenza A virus nucleoprotein stain and resulting binary readouts (blue = positive, yellow = negative) generated by automated image processing at increasing virus stock dilution factors of 10^{-2}, 10^{-3} and 10^{-4} (MM overlay, 3 replicates for each case shown). (B) Microwell fractions exhibiting positive infection using MCC and MM overlays for each viral stock dilution (n=3 for each case). The error bars in the boxplots represent the variation in data between the replicate chips at each condition, with the box bounding the data between the first and third quartiles, while the whiskers on either end span 1.5 times the interquartile range. 34
Figure 2.11. Viral titers determined from dFA and plaque assay. Measured viral titers determined by the digital focus assay when utilizing different initial dilution factors. Assay results are presented for both MCC and MM overlays, and compared with the readout from a plaque assay for the same viral stock. The error bars in the boxplots represent the variation in data between the replicate assays at each condition (n=3), with the box bounding the data between the first and third quartiles, while end whiskers span 1.5 times the interquartile range. Solid and dashed lines represent median and mean viral titers, respectively. A Z-test was applied to compare each dFA distributions against the reference plaque assay, yielding Z-scores between 0.07-1.5..... 37
Figure 2.12. Fluorescence images and automated dFA readout for nasal swab specimens. Images and binary readout for a subset of wells in each of 3 replicate chips run on nasal swab specimens with high (sample 1) and low (sample 2) viral titer. Both samples were evaluated without dilution. 42
Figure 3.1. Measurement of the SU-8 mold for the planar flow-focusing droplet generators using an optical profilometer, showing a feature height of 25 µm, the x- and y-profiles, and a 3D contour model of a single device. 49
Figure 3.2. Microfluidic planar flow-focusing droplet generators: (A) 15 µm-orifice devices generating monodisperse emulsions with a mean droplet diameter of 12.5 µm; (B) 30 µm-orifice devices generating monodisperse emulsions with a mean droplet diameter of 18 µm, shown 24 hours after the start of droplet production..... 51

Figure 3.3. Image sequence showing sedimentation of droplets in a water-in-oil emulsion over discretized 200 µm microwells prefilled with water, captured at (A) 0 minutes, (B) 5 minutes, (C) 15 minutes, and (D) 30 minutes after initial discretization. 53
Figure 3.4. Image sequence showing droplet merging of the emulsion with discretized microwells, captured at (A) 0 minutes, (B) 20 minutes, (C) 45 minutes, (D) 55 minutes, (E) 60 minutes, and (F) 75 minutes after the start of surfactant-free oil flow into the chip at 0.2 µL/min. The oil flows from left to right in each image. Due to the pulsatile nature of the oil flow, sedimented droplets are better retained and less susceptible to loss from drag and lift forces. 55
Figure 3.5. Schematic of the functionalized magnetic bead-based sandwich assay. NHS-activated beads are functionalized with a primary antibody (mouse anti-HA monoclonal antibody) and loaded into the microwells, where they are secured in place using an external permanent magnet. PR8 influenza virus is delivered to the microwells through droplet merging. A rabbit anti-HA polyclonal antibody is then flowed into the device, binding to multiple epitopes on the captured PR8 virus particles. Finally, a goat anti-rabbit IgG polyclonal antibody conjugated to a fluorophore is introduced, binding to the immobilized rabbit antibodies and enabling visualization of the captured virus through signal amplification. 56
Figure 3.6. Fluorescence intensity of stained functionalized magnetic beads as a function of viral load. Images show fluorescence from beads incubated with (A) 5E3 FFU/mL, (B) 5E2 FFU/mL, and (C) negative control (0 FFU/mL). 58
Figure 3.7. (A) Microscopy image showing aerosols collected as droplets in oil using the BioSpot VIVAS condensation growth tube system, sampled over 60 minutes. (B) Corresponding size distribution histogram. (C) Microscopy image showing aerosols collected as droplets in oil using the BioSpot VIVAS condensation growth tube system, sampled over 90 minutes. (D) Corresponding size distribution histogram. 61
Figure 3.8. (A) Representative image of droplets in emulsion sedimented over a discretized microwell array. (B) Image analysis of (A) showing the number of droplets in each ROI corresponding to a single microwell. (C) Droplet count histogram (bin size = 5) showing the distribution of droplets across the array. (D) The same data visualized as a heatmap, with droplet counts overlaid on individual ROIs. 62
Figure 3.9. (A) Sedimented PR8 virus-containing droplets over discretized microwells loaded with functionalized magnetic beads. (B) Microwell array after completion of droplet merging, showing dewetting but no loss of magnetic beads. (C) Fluorescence microscopy image of the microwell array after antibody staining post-droplet merging, where the delivered droplets contained virus at 5E4 FFU/mL. (D) Fluorescence microscopy image of the microwell array after antibody staining for a negative control device post-droplet merging, where the delivered droplets contained no virus..... 67
Figure 4.1. Image of the prototype dFA chip with reservoirs over the inlet and outlet ports to hold excess media and oil, preventing chip dry-out..... 74

List of Abbreviations

CGT	Condensation Growth Tube
dFA	Digital Focus Assay
DMEM	Dulbecco's Modified Eagle Medium
FFA	Focus Forming Assay
FFU	Focus-Forming Unit
HA	Hemagglutinin
hCK	Humanized MDCK cells
HLB	Hydrophilic-Lipophilic Balance
IAV	Influenza A Virus
IRP	Infectious Respiratory Particle
MCC	Microcrystalline Cellulose
MDCK	Madin-Darby Canine Kidney cells
MM	Maintenance Medium
NA	Influenza Virus Nucleoprotein
PBS	Phosphate-Buffered Saline
PCR	Polymerase Chain Reaction
PDMS	Polydimethylsiloxane
PFU	Plaque-Forming Unit
PR8	Influenza A virus A/Puerto Rico/8/1934 (H1N1)
ROI	Region of Interest

Chapter 1: Background

Motivation

Influenza is an acute respiratory infectious disease caused by the influenza virus. It is responsible for seasonal epidemics and occasionally leads to pandemics. Influenza, or more commonly referred to as the "flu", is both an anthroponotic and a zoonotic disease, in that it can be transmitted from human to human as well as from animals to humans, primarily from birds and mammals. Influenza viruses can be classified into four types: A, B, C, and D, based on antigenic differences. Influenza A and B viruses are mostly responsible for seasonal epidemic outbreaks in humans, while influenza A viruses of zoonotic origin that can infect and spread among humans, to which humans have no immunity, have been responsible for pandemics in the past.[1]

Influenza is primarily transmitted through respiratory droplets and aerosols, and less commonly through contaminated surfaces. The onset of symptoms typically occurs around two days after infection. While most people recover from the illness without medical supervision, infections in vulnerable populations can lead to higher levels of morbidity and mortality. Vulnerable populations include the elderly aged 65 and above, children under the age of five, individuals with chronic medical illnesses, and immunocompromised individuals.[2]

According to the United States Centers for Disease Control and Prevention (CDC), between the years 2010 and 2024, there were 9.3 to 41 million cases of influenza

infections in the United States annually, leading to 120,000 to 710,000 hospitalizations and 6,300 to 52,000 deaths.[3] Based on the preliminary in-season report of the 2024-2025 season from the CDC, for data collected between October 1, 2024, and May 17, 2025, the flu was responsible for up to 82 million cases of illness, leading to up to 1.3 million hospitalizations and up to 130,000 deaths.[4]

Globally, according to the World Health Organization (WHO), there are around one billion cases of influenza each year, leading to up to five million cases of severe illness and up to 650,000 deaths.[2] Influenza A viruses have also been responsible for four major pandemics since 1900, including the Great Flu Pandemic of 1918, more commonly known as the Spanish flu pandemic, which infected one-third of Earth's population and resulted in about 50 million deaths.[5] In temperate climates, such as in most of the United States, seasonal influenza outbreaks occur during the winter, while in tropical regions, infections occur year-round and outbreaks are irregular.

Given the significant global and domestic health impacts of influenza, accurate quantification of viable virus plays a critical role in understanding transmission dynamics, assessing disease severity, and guiding prevention and treatment strategies. Quantification of viral titer is important for a wide range of applications in infectious disease research. For example, characterization of viral load over time is necessary for establishing infection kinetics, [6–12] improving the fundamental understanding of disease progression by informing dynamic models of virus replication within host cells [13], and identifying host cellular factors required for viral replication [14,15]. Viral titer

quantification is also critical for epidemiology and viral transmission studies [16–22], characterizing the relative pathogenicity of viral strains [21], and evaluating the mechanism and efficacy of antiviral treatments.[23–31] In addition, quantifying infectious virus is important in the development of novel vaccine candidates, [32–35] testing newer methods of vaccine production [36–39], and evaluating vaccines for safety and efficacy [40–43]. It also finds application in newer areas of research such as in the production of recombinant adeno-associated virus (rAAV)-based gene therapy, where the infectious titer of the AAV particles is important to determine the efficacy of the product and thereby the potency of AAV-based gene therapy. [44–46] Measurements of viral titer can also play a role in clinical settings as an approach to assessing the severity of infection. [47–49]

The most common methods used for virus quantification are nucleic acid amplification tests (NAATs) including polymerase chain reaction (PCR) and loop-mediated isothermal amplification (LAMP). These assays can confirm the presence of virus-specific nucleic acids [16,19,20,50–55], while serological assays like the enzyme-linked immunosorbent assay (ELISA) can be designed to test for viral antigens such as the influenza A nucleoprotein [56–59] or measure the level of virus specific antibodies in that are produced in response to an infection or vaccination [60–62]. However, immunoassays can yield false-negative results due to the limited window of detection [63] and are less sensitive than NAATs [64]. Furthermore, like NAATs, they only provide a correlation to the infectious viral load and cannot be used to determine if functional viral particles are present. This is notable, since in the case of influenza virus, less than 1 % of the total

virus particle count has been reported to be infectious[51] and the infection generation rate might be 1/300th of the total number of viral copies detected by PCR.[19,52,53]

Unlike NAATs and immunoassays, cell-culture based assays can provide direct measurements of viable virus by quantifying individual cell inoculation events leading to virus expansion. The plaque assay is considered a gold standard[65] that provides a simple and inexpensive approach to quantifying viable virus through the counting of dead cell plaques that form in a monolayer cell culture after viral inoculation.[66,67] However, plaque assays suffer from several drawbacks including long assay times of at least 2-3 days, labor intensive operation, subjectivity in counting plaques, and poor performance when evaluating viruses that generate small and/or unclear plaques, or simply no plaques at all.[68–70] Furthermore, plaque assays can be unreliable when other sources of cytotoxicity are present in the sample, such as in clinical settings where an individual may carry multiple agents capable of causing cytopathic effect (CPE) in host cells.

One alternative to the plaque assay is the Median Tissue Culture Infectious Dose ($TCID_{50}$) assay. This assay is also cell-culture based, but quantifies viable virus by determining the dose required to infect half of the inoculated wells.[70–72] Still, as with plaque assays, $TCID_{50}$ assays are time consuming, with a 3-5 day turnaround for influenza A [70,71]. Thus, another option is the focus-forming assay (FFA), which is a variation of the plaque assay in which viable virus is quantified through the counting of foci of infected cells that are visualized after staining with a virus-specific antibody.

In addition to providing higher specificity though the use of antibody labeling, the FFA offers higher sensitivity than plaque assays together with the ability to quantify non-lytic viruses [73]. It is also considerably faster than a plaque assay (e.g. 8-24 hours [74] vs. 3 days [75] in the case of influenza virus). However, the FFA assay cost is relatively high due to the fluorescent dyes and antibodies required for staining [73], and assay endpoint times must be optimized for a given virus strain and cell line, since shorter incubation times suffer from undercounting of foci [76,77] while longer incubation times can lead to undercounting due to the merging of foci [77]. In addition, while the FFA readout analysis can be automated through the use of specialized instrumentation, manual counting is typically employed, introducing subjectivity in distinguishing between small foci and visual artifacts. [78]

Aerosol Sampling Methods for Studying Viral Distribution and Viability

Beyond direct quantification in cell culture, characterizing the distribution and infectious potential of viruses within airborne particles is essential for improving our understanding of respiratory infections. Respiratory particles carrying pathogen are emitted when an infected person coughs, sneezes, talks, or breathes[79] and can depend on various factors such as the ambient temperature and humidity. Historically, transmission was described as occurring via “droplets” (>5 μm) that were thought to settle within 1–2 meters, and “aerosols” (<5 μm) that were thought to remain suspended and reach the alveoli. This framework is now recognized as incorrect.[80] The WHO emphasizes that a new term "infectious respiratory particles" (IRP) be used for particles in a continuum of sizes with no sharp cutoffs rather than "aerosol" or "droplets".[81]

Airborne transmission, defined as the inhalation of IRPs, can occur at any distance from the source, and inhaled particles can deposit throughout the respiratory tract rather than being restricted to the alveoli. In contrast, direct deposition occurs when larger IRPs follow semi-ballistic trajectories to land directly on the mucosa of the eyes, nose, or mouth. The concentration of IRPs is highest close to the source, where they exit the respiratory tract, and decreases with distance as larger particles fall out and smaller ones are diluted in the surrounding air. In enclosed or poorly ventilated environments, smaller IRPs can accumulate over time, creating elevated risks of transmission even in the absence of close contact. As a result, understanding this full spectrum of particle behavior is critical for studying viral distribution and transmission.

Single-aerosol analysis provides new opportunities to address fundamental questions in aerovirology that traditional bulk assays, which homogenize samples in aqueous media, cannot resolve. Influenza infections in host cells often require more than one virus particle to establish productive infection. One important reason is that Influenza A virus, with its segmented genome, frequently produces incomplete particles, making co-infection by multiple virions necessary for the delivery of complementary genomes to initiate infection and replication. Conventional aerosol sampling techniques cannot determine how complete and incomplete genomes are distributed across individual aerosol droplets because they homogenize samples in aqueous collection media. Therefore, development of a technology is needed that can collect aerosols as discrete particles and analyze their composition at the single-particle level, which would enable insights into how many particles, and what combinations of particles, are required to

drive transmission. While size-fractionation methods can reveal which droplet sizes are capable of carrying virus, they cannot capture the heterogeneity within droplets of the same aerodynamic size. Single-aerosol analysis resolves this compositional variability, showing that droplets of identical size can differ substantially in viral content. These insights deepen mechanistic understanding of how viruses are packaged and transmitted through aerosols, improve the accuracy of transmission models, and inform the design of more targeted intervention strategies.

Some of the established methods of collection of exhaled breath and environmental aerosols today include impactors,[82] liquid impingers,[83] electrostatic precipitators,[84] water-based condensation growth tube collectors,[85] personal cyclone-based aerosol samplers such as the NIOSH two-stage bioaerosol sampler, which can collect aerosols from the ambient environment at different size fractions at a low flow rate of 3.5 L/min,[86] and devices such as the Gesundheit-II (G-II), which collect aerosols from human subjects performing various respiratory maneuvers at high flow rates of nearly 130 L/min and are capable of capturing fine and coarse aerosols over 50 nm with high collection efficiencies.[87] Conventional methods of airborne virus collection present several challenges, including loss of viability from dehydration, re-aerosolization, and impact forces.[88] In addition, it remains unclear how virus viability is affected in collection media outside the native aerosol components such as mucus, proteins, surfactants, and salts. Water-based laminar flow-condensation growth tubes (CGTs) that grow aerosols by condensing water on them were found to be more efficient in collection of airborne virus[85] and help maintaining their viability[89]. They can be

portable and operate by passing cooled aerosols through warm, supersaturated columns, with final droplet size tuned by adjusting flow and temperatures in different sections of the column. Studies have demonstrated that commercial CGTs like the BioSpot-VIVAS, have been successful in reliably capturing airborne bacteria and yeast,[90] influenza,[85,91] and SARS-CoV-2 virus[92–94] with high rates of viability. While VIVAS, when coupled with instruments such as the BioCascade Impactor,[95,96] can enable analysis of various size fractions of airborne particles, they are limited by the fact that samples are collected in aqueous media such as nutrient solutions or virus transport media (VTM), which homogenize the particles before analysis and make it difficult to study the distribution of the virus among droplets within each size fraction. To address this limitation, impactors and CGTs can be modified to replace the traditional aqueous collection medium with an immiscible, biocompatible liquid such as mineral oils or fluorinated oils, which preserves the integrity of individual droplets. These discrete droplets can then be directly analyzed to determine their contents, enabling detailed investigation of virus distribution across droplets and contributing to a better understanding of the quanta of infection, a concept that remains poorly understood in aerovirology. CGTs coupled with an upstream impactor are particularly advantageous for this application, as they can selectively enlarge submicron particles while they pass through successive stages of the tube. BioSpot VIVAS, a CGT-based aerosol collection system that was designed and developed by Aerosol Devices, and used in this dissertation for aerosol collection is shown in Fig. 1.1. By controlling and optimizing temperature and humidity in different sections, the particles can be grown

by water condensation to a narrow size range of 1-3 μm,[97] or larger by adjusting the initiator temperature,[98] and then collected in oil through gentle impaction.

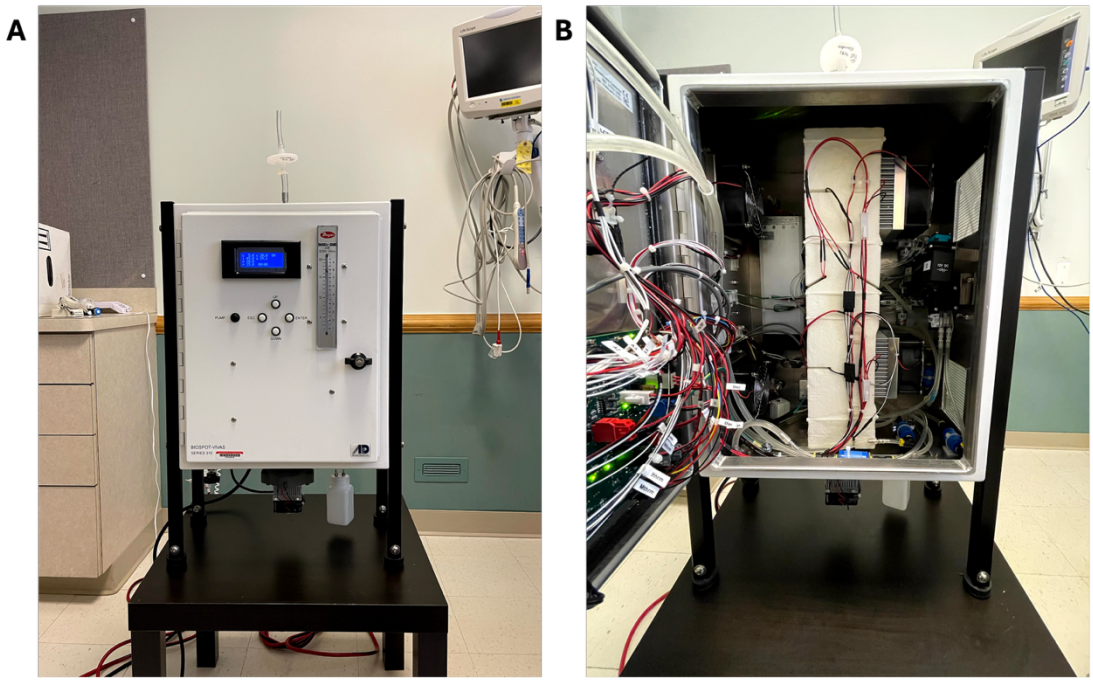


Figure 1.1. (A) The BioSpot VIVAS, a condensation growth tube (CGT)-based aerosol sampler developed by Aerosol Devices and used in this dissertation for aerosol sampling experiments. (B) The BioSpot VIVAS with the front door open, showing the condensation growth tube and the temperature-controlled zones of the wetted wall column.

Microfluidic emulsion generation for viral aerosol modeling

While aerosols can be collected as water-in-oil emulsions using the condensation growth tube, the collection process requires fine-tuned control and optimization. In this work, to study the downstream delivery of viruses in droplets through droplet merging, synthetic model emulsions were used instead. The model emulsions were created using a microfluidic planar flow-focusing device.

Emulsification to create water droplets in oil can be achieved either through top-down or bottom-up approaches. Top-down emulsification involves using turbulence to break up water into droplets, but there is little control over the size and distribution of the droplets formed. Microfluidics is well established in the literature for bottom-up emulsion formation, creating monodisperse droplets. There are various established methods for creating these droplets using microfluidics, which can be divided into two major categories: active and passive. While there is no consensus in the literature on the exact definitions of active and passive modes of droplet generation, active droplet generation typically involves the use of external forces such as electrical fields, magnetic fields, thermal energy, and mechanical control using pneumatic or piezoelectric systems.[99,100] Advantages of active methods include fast response times, precise on-demand control, and the potential for higher throughput. Passive modes of droplet generation, on the other hand, rely on the inherent fluid dynamics and geometry of the microfluidic channel. The most common architectures for passive droplet generation are the T-junction[101] and flow-focusing designs.[102]

T-junctions use crossflow, with oil and water streams intersecting orthogonally. The T-junction has a simple design and can produce monodisperse droplets with little variation. Parameters that can be controlled to modify droplet size and throughput include the geometries of the microchannels, the total flow rate, and the flow rate ratio of the two immiscible phases. However, T-junctions have drawbacks, including limitations in producing smaller droplets and lower total throughput since droplets are

generated sequentially, one at a time. This makes flow focusing a better alternative for producing smaller droplets at higher throughput.

Flow focusing can be further classified into 3D axisymmetric[103,104] and 2D planar configurations[105,106]. 2D planar flow-focusing devices have the advantage of simpler design and fabrication through patterning on silicon wafers using photolithography, followed by soft lithography.[106] To produce a water-in-oil emulsion using the planar flow-focusing microfluidic device, water is flowed into the central channel and oil into the two outer channels. The flows are forced through a small orifice downstream of the three channels. As the streams pass through the orifice, the viscous stress from the oil flow in the outer channels causes the central water stream to break into droplets. The size and throughput of the droplets can be controlled by adjusting the total flow rates of the water and oil streams and the flow rate ratio between the two phases.

To enable downstream analysis of viral aerosols in this dissertation, a platform capable of generating monodisperse droplets in a controlled manner was essential. Microfluidic flow focusing devices provided a robust solution by offering precise control over droplet size, stability, and throughput, making them ideal for generating synthetic model emulsions.

Influenza remains a major public health concern due to its ability to spread rapidly and cause substantial morbidity and mortality. Although current methods for quantifying infectious viral particles are well established, they often fall short in terms of speed,

sensitivity, and ease of use. This dissertation presents two complementary approaches to address these limitations. Chapter 2 presents the development of a digital focus assay for rapid, cost-effective, and user-friendly quantification of viable influenza virus. In Chapter 3, progress toward the development of an analytical strategy combining aerosol collection, microwell array discretization, and controlled droplet merging is presented as a unique approach for evaluating the distribution of viruses within airborne droplets. Finally, Chapter 4 describes future opportunities for improving the performance of the digital focus assay technology and advancing the droplet merging platform for single-aerosol analysis.

Chapter 2: Microfluidic digital focus assays for the quantification of infectious influenza virus

Digital assays employ large numbers of discrete sample volumes where dilute assay targets are distributed across these volumes. The target concentration within the initial sample can then be determined by evaluating the fraction of volumes containing at least one target and assuming a Poisson distribution across the volumes. Digital assays employing droplets or microwell arrays for sample discretization have been broadly successful for nucleic acid quantification, with microfluidic digital PCR [107–109] and digital LAMP [110,111] being widely used for absolute quantification of nucleic acids with high sensitivity. Taking inspiration from digital NAATs, the digital focus assay (dFA) described here discretizes a virus-containing sample into a microwell array culture platform, with viral titer determined by evaluating the fraction of wells where viral replication occurs. To prevent cross-talk between adjacent microwells, which would compromise assay readout [112], an immiscible oil phase is used to discretize the microwells [113–115]. While a conventional FFA requires foci counting to be performed within an optimal time window to ensure sufficient virus expansion for detection while avoiding excessive growth and subsequent overlapping of individual foci, the dFA employs mineral oil to discretize the microwells and prevent cross-talk between the well volumes, allowing the viral titer to be calculated through binary readout from individual wells after extended replication, with indirect quantification based on statistical analysis. As with a conventional FFA, the dFA was found to be significantly faster than a plaque assay while providing a high level of specificity to the virus through

immunofluorescent staining and removing the requirement for the virus to cause CPE in the host cells.

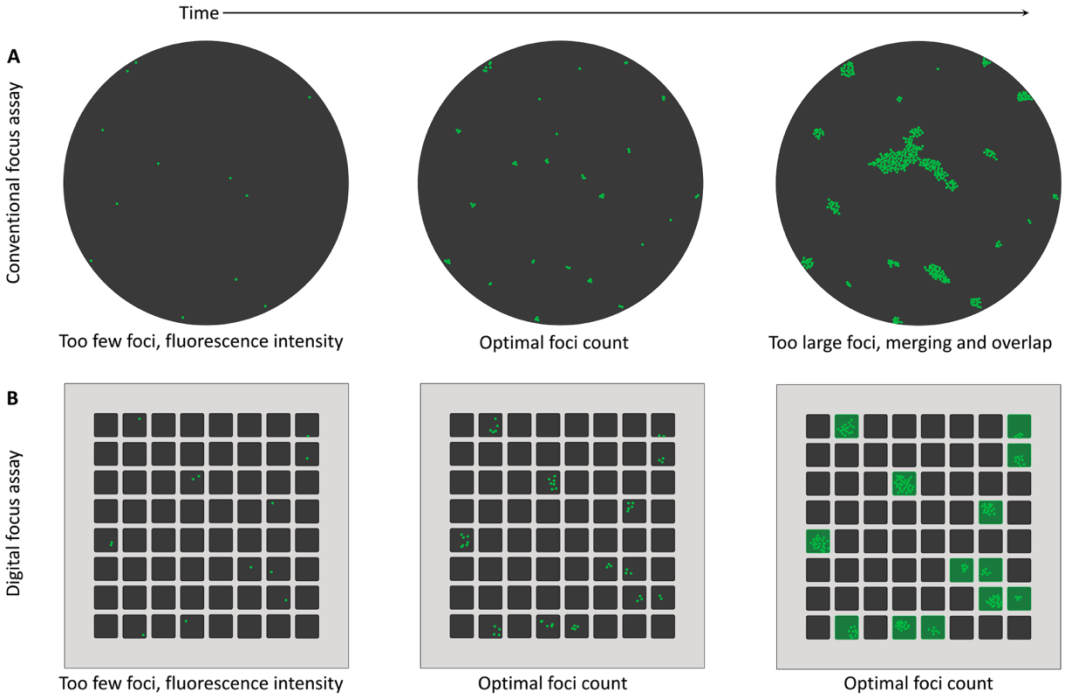


Figure 2.1. Conceptual comparison of conventional and digital focus assays for infectious virus quantification. (A) In a conventional FFA, assay readout is performed in a narrow time window following primary infection but before excessive replication can occur to ensure the growth of small discrete foci for quantification. (B) The digital focus assay sequesters virus within a large number of discrete microwells, enabling binary readout from individual wells after extended replication with indirect quantification based on statistical analysis.

The microfluidic architecture of the dFA serves to reduce reagent and sample consumption by approximately 10-fold, reducing reagent costs compared with conventional FFAs while also making the platform compatible with highly limited sample volumes. Significantly, the digital nature of the platform isolates discrete infection events, allowing flexible incubation times without concern over excessive growth of foci that would otherwise add uncertainty to assay readout. Furthermore, the assay process including sample introduction and immunostaining is convenient and

straightforward, and image analysis for digital readout is readily automated without the need for specialized instrumentation. Fig. 2.1 summarizes the conceptual difference between a conventional focus-forming assay and the microfluidic digital focus assay for infectious virus quantification. Performance of the dFA platform is investigated for the quantification of influenza A virus, with viral titer measurements found to be in good agreement with a paired plaque assay making it a feasible, rapid, convenient, and cost-effective platform for the quantification of viable virus.

Experimental

Device Design and Fabrication

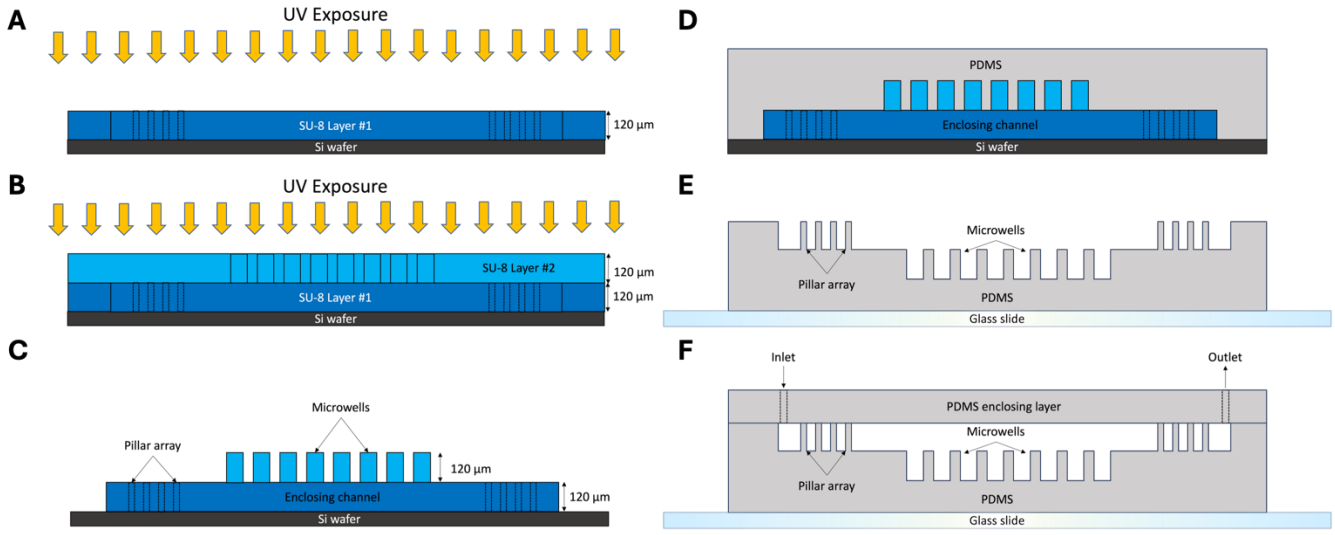


Figure 2.2. Fabrication schematics of the SU-8 master mold and the PDMS microfluidic device. (A) 120 µm SU-8 2075 is coated on a 4" Si wafer and patterned through photolithography (B) After a short post-exposure bake, a second layer of SU-8 was coated on top and patterned through photolithography (C) The unexposed SU-8 was developed away completing the fabrication of the mold (D) 10:1 PDMS was poured over the SU-8 mold and cured at 80 °C for 3 hours (E) The cured PDMS was cut and bonded to a 3" glass slide through oxygen plasma activation (F) An unpatterned PDMS block with holes punched for inlet and outlet ports was bonded over the patterned microwell PDMS layer, completing the PDMS device fabrication

Devices were fabricated through PDMS soft lithography using multi-layered photoresist molds prepared by adapting a reported technique [116] and the fabrication process schematics are depicted in Fig 2.2. Briefly, a 110 μm thick layer of SU-8 2075 photoresist (Kayaku Advanced Materials) was spin coated on a 4" silicon wafer (University Wafer). The coated wafer was soft-baked and the design corresponding to the channels and the pillar arrays for mixing were exposed using a maskless aligner (MLA 150, Heidelberg Instruments). Following a short post-exposure bake at 65 °C for 60 s, a second layer of 110 μm SU-8 was spin coated over the initial SU-8 layer. The spin speed employed for the second SU-8 film was 1.2 times higher than the spin speed employed on the bare silicon surface [116]. The wafer was then soft-baked at 65 °C for 5 min followed by 95 °C for 20 min before mask alignment and UV exposure to pattern the microwell array. Following a post-exposure bake, development, and a hard-bake the final multi-layer SU-8 mold was ready for PDMS soft lithography. A separate single-layer SU-8 mold containing alignment marks for fluidic access ports was prepared using the above steps for fabrication of the sealing layer.

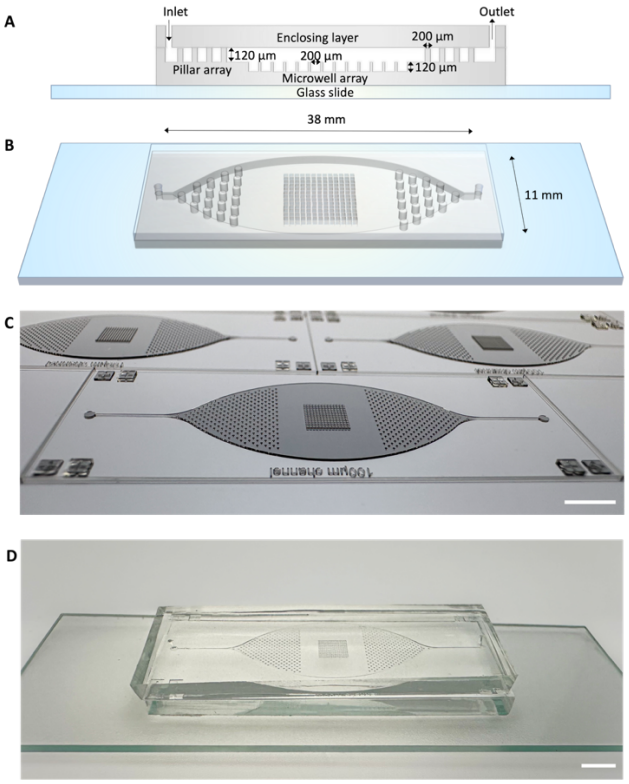


Figure 2.3. Overview of the dFA chip geometry. (A) Cross-sectional schematic of a PDMS chip bonded to the glass slide, with feature dimensions indicated. (B) Perspective view of a chip revealing the 13x13 microwell array and enclosing channel with inlet and outlet pillar arrays designed for improved cell seeding uniformity. (C) Image of a fabricated multi-layer SU-8 patterned wafer with 8 devices per mold. D) An image of the enclosed PDMS microwell array chip. Scale bar: 4 mm.

PDMS (Sylgard 184, Dow) was prepared by mixing the base prepolymer and the crosslinker (10:1 weight ratio). Next, 1 µL of saturated Pluronic F-108 (Sigma Aldrich) solution in ethanol (200 mg/mL) was added to every 1 g of the PDMS prepolymer and mixed together to support hydrophilic modification of the final PDMS surfaces [117]. The mixture was degassed and then poured onto the multi-layered SU-8 microwell mold. It was cured at 80°C for 3 h and peeled from the mold. Blocks corresponding to a single device were cut and bonded to a 1”x3” glass slide (AmScope) through oxygen plasma activation of the surfaces at 200 W for 30 s (PE-25, Plasma Etch). Similarly, cured

PDMS blocks for the enclosing layer were cut and holes punched for fluidic access using a 0.5 mm ID biopsy punch tool (World Precision Instruments), and bonded to the base PDMS layer through oxygen plasma activation. Sterile 24 gauge blunt-tip needle segments (SAI Infusion Technologies) were inserted into the fluidic access holes to enable the connection of flexible Tygon tubing (0.020" ID x 0.060" OD, Masterflex) for interfacing between the chip and a syringe pump (Fusion 100, Chemyx) for injection of fluids into the chip using 1 mL syringes (BD Luer-Lok).

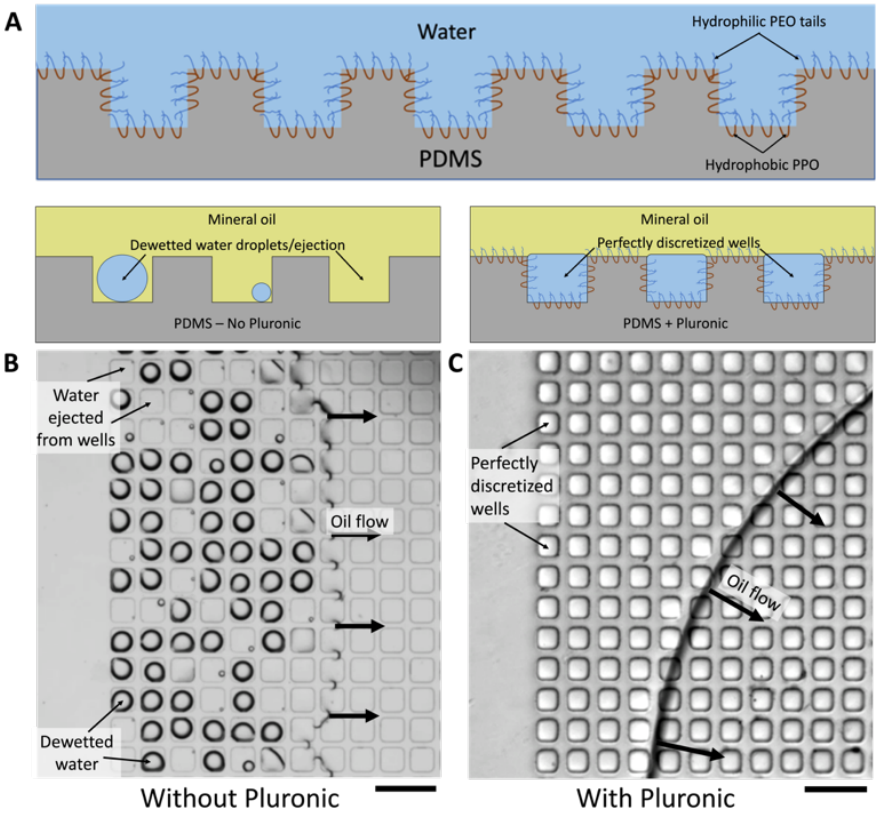


Figure 2.4. Hydrophilic surface modification through embedded Pluronic surfactant. (A) Pluronic F-108 embedded into the PDMS matrix yields a hydrophilic surface after overnight exposure to water. (B) Cross-sectional schematic and image of the 200 µm PDMS microwells without embedded Pluronic F-108. Flowing mineral oil over the microwells prefilled with water caused dewetting and partial ejection of water from the microwells. (C) Cross-sectional schematic and image of the 200 µm PDMS microwells with embedded Pluronic F-108. Flowing mineral oil over the microwells yields perfect discretization of the microwells without observable loss of water. Scale bar: 500 µm.

Following fabrication, deionized water was perfused through the chip, and the water-filled device was placed under a vacuum for 2 min to displace air from the microwells to ensure complete filling of the microwells with water. The water-filled chip was then incubated in a refrigerator at 4 °C for at least 24 h to facilitate the migration and reorientation of Pluronic F-108 molecules within the PDMS matrix to present hydrophilic domains at the exposed surfaces. Because the PDMS was observed to gradually recover its hydrophobicity over time, all chips used in this dissertation were stored under water at 4 °C to slow the surface recovery process, and cell culture was initiated within a week of device fabrication.

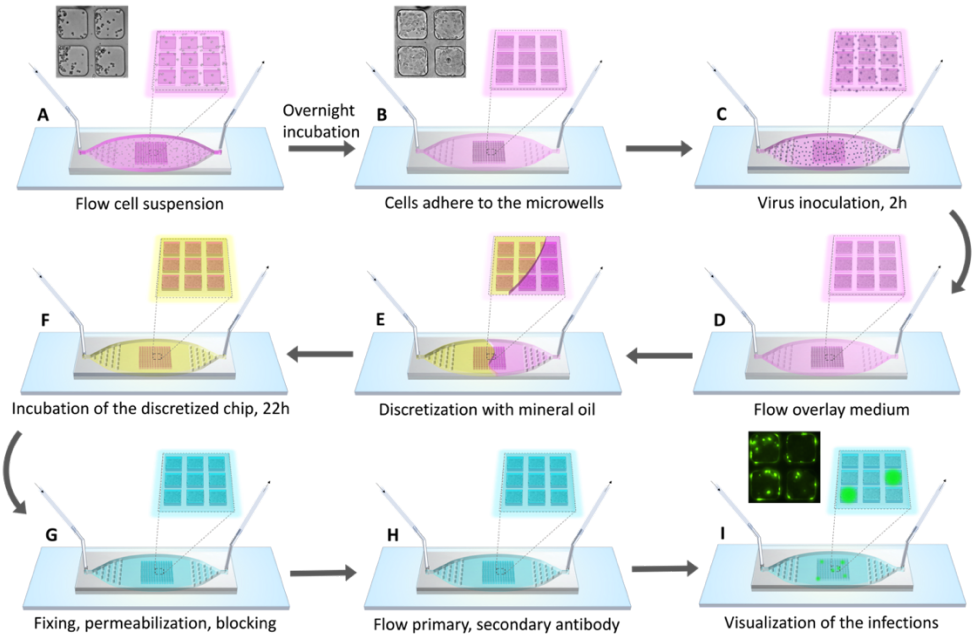


Figure 2.5. Digital focus assay process. (A) As MDCK cell suspension flows into the chip, the cells sediment into the microwells and adhere to the walls after incubation at 37 °C with 5% CO_2. (B) Overnight incubation resulted in nearly confluent MDCK cell growth within individual microwells. (C) Influenza A virus inoculum is introduced into the chip and incubated for 2 h. (D) Overlay medium is introduced into the chip that flushed out any unadsorbed virus from the chip. (E) Mineral oil is introduced into the chip to discretize the microwells and prevent cross-contamination between their volumes. (F) Discretized microwell arrays containing the cultured MDCK cells inoculated with influenza A virus and filled with an overlay medium are incubated for 22 h. (G-I) The oil and overlay media are flushed out with PBS at the end of the assay to permit fixing, permeabilization, and immunofluorescent staining of the cells.

Cell Seeding

The first step for performing the dFA was seeding of Madin-Darby Canine Kidney (MDCK) cells into the microwells. A 50 µL suspension (10^6 cells/mL) of MDCK cells in culture medium (DMEM, high glucose, pyruvate, Gibco) supplemented with 10% fetal bovine serum (FBS) (Thermo Fisher Scientific) and 1x Penicillin-Streptomycin (Thermo Fisher Scientific) was injected into the device. The cells were allowed to sediment into the microwells over a period of 2 min with the flow stopped. This seeding process was repeated until the desired cell density was reached in the microwells. At the end of the cell seeding step, 50 µL of cell-free medium was flowed into the device to nudge any cells that had sedimented in the plateau region between the microwells into the nearest microwell. This step also ensured the removal of cells from other parts of the channel, leaving the cells contained only within the microwell array. The chips were subsequently placed overnight in an incubator at 37 °C with 5% CO_2 to facilitate the adhesion and growth of the MDCK cells on the base and walls of the microwells. Fig. 2.6 shows the progression of the seeded MDCK cells in PDMS microwells from 0-24 hours.

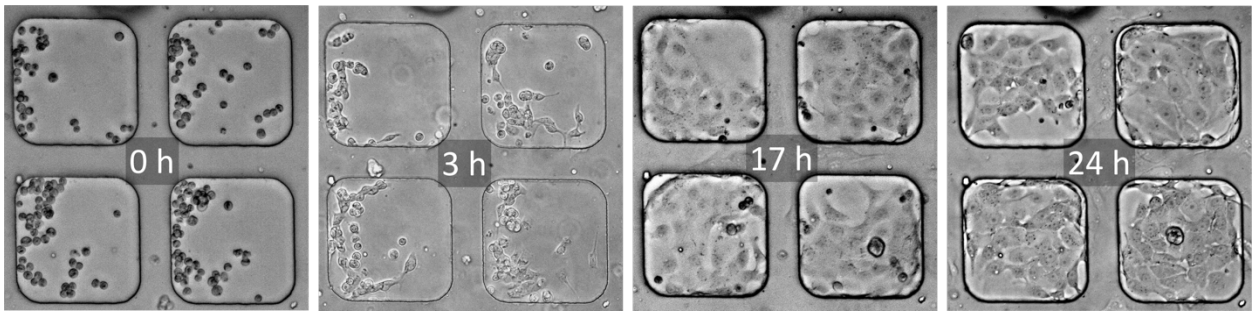


Figure 2.6. Images showing the MDCK cell culture progression from 0-24 hours within PDMS microwells

Virus Inoculation and Well Discretization

A laboratory stock of the influenza A virus (A/Perth/16/2009(H3N2)), produced by plasmid transfection in 293T cells and subsequent coculture with MDCK cells, was serially diluted in serum-free DMEM giving 500 µL of the virus inoculum each at 10^{-2}, 10^{-3} and 10^{-4} dilution factors. Prior to introducing the influenza virus inoculum, the chip was flushed with serum-free DMEM to remove all FBS from the microwells. A 60 µL suspension of virus inoculum at each dilution factor was injected into each chip and incubated at 37 °C with 5% CO_2 to facilitate the adsorption and attachment of the influenza virus to the MDCK cells. After 2 h incubation, an overlay media consisting of either maintenance media (MM) (DMEM/Nutrient Mixture F-12 Ham with L-glutamine, 15 mM HEPES, and sodium bicarbonate, Sigma Aldrich) containing 1.5 µg/mL TPCK-treated trypsin (Thermo Fisher Scientific) or 0.6% microcrystalline cellulose (MCC) (Sigma Aldrich) in the aforementioned MM was perfused through the chip at a flow rate of 100 µL/min. TPCK-treated trypsin was added to the medium because it cleaves the hemagglutinin (HA) protein at its activation site to generate infectious virions. This step ensures the production of infectious progeny viruses in each microwell from the initial infection event, thereby allowing secondary infection to occur and making infection more readily identifiable through downstream immunostaining. In addition to providing an appropriate environment for cell culture, the overlay flow served to facilitate removal of any unbound virus from the upper plateau region of the microwell chip. Mineral oil (Light mineral oil, Sigma Aldrich) was next introduced at a flow rate of 50 µL/min into the chip to discretize the

microwells, while retaining the overlay medium in each microwell owing to the hydrophilic modification through the embedded Pluronic. The oil-discretized chip was then placed in an incubator at 37 °C with 5% CO_2 for an additional 22 h to support replication and spread of the progeny influenza virus within individual microwells.

Fixing and Staining

At the end of the infection incubation, the chips were flushed with phosphate-buffered saline (PBS) to remove all oil and overlay medium. To visualize infected cells, 60 µL of 4% paraformaldehyde (PFA) (Electron Microscopy Sciences) in PBS was flowed into each chip and incubated for 10 min to fix the cells. The PFA was flushed out by flowing PBS + 0.1% Tween 20 (PBS-T) into the chip. The PBS-T also helped to remove any residual mineral oil from the channels and the microwells. The cells were then permeabilized by flowing 2.5% Triton-X in PBS to facilitate detection of intracellular targets. Cells were incubated for 15 min and then washed by flowing PBS into the chip. Blocking was performed by flowing 3% bovine serum albumin (BSA) (Sigma Aldrich) in PBS, preventing non-specific binding and thereby reducing background noise in the subsequent staining steps. After incubating for 1 h at room temperature, the blocking solution was flushed out by flowing PBS into the chip. A 60 µL volume of primary antibody (mouse anti-influenza A antibody, nucleoprotein, clones A1, A3 Blend, Sigma Aldrich) diluted 1:100 in PBS with 1% BSA was introduced into the chip and incubated at 4 °C overnight. Following a thorough wash with PBS, secondary antibody (donkey anti-mouse IgG, Alexa Fluor 488, Thermo Fisher) diluted 1:500 in PBS was flowed through the chip and incubated at room temperature for at least 1 hour. Following a thorough wash with PBS, 1 µg/mL of

nuclear stain (Hoechst 33258, Pentahydrate (bis-Benzimide), Thermo Fisher) was flowed into the chip and incubated for 10 min before thoroughly washing away unbound dye with PBS. The chip was then visualized using epifluorescence microscopy (Nikon ECLIPSE Ti2-E) and images of the full microwell array were captured (pco.edge 4.2 bi USB sCMOS Camera).

Image analysis to determine the distribution of cells across the microwells through the Hoechst nuclear stain, as well as the distribution of viral antigen-positive cells through immunofluorescent staining, was automated using custom Python code. For final assay readout, raw fluorescence microscopy images were converted to an 8-bit grayscale format and divided into regions of interest (ROIs) aligned with the 13x13 array of microwells. A pixel intensity threshold was applied to each ROI to remove background fluorescence, and regions with at least 10 contiguous pixels above the threshold value were interpreted as a positive infection event.

Clinical Specimen Analysis

Nasal swab samples were collected from a volunteer donor participating in a clinical research study approved by the University of Maryland Baltimore Institutional Review Board (HP-00103865), with an acute influenza A infection, confirmed by Cepheid Xpert Xpress CoV-2/Flu/RSV plus tests. Two samples were collected on subsequent days and separated into two fractions, with one fraction used for dFA assays and the second fraction reserved for digital PCR (dPCR) analysis. For dFA analysis, buffer containing TPCK-treated trypsin and antibiotics was added to the undiluted sample for a 9:1 ratio of sample:buffer, and each sample was run independently on 3 replicate dFA

chips. Cell seeding in the dFA chips followed the same procedure used for the model virus experiments, but with MDCK cells replaced with humanized MDCK (hCK) cells that are genetically engineered to express higher levels of human influenza virus receptors, making them more susceptible to infection by currently circulating wild-type influenza virus [118]. Influenza A viral loads in clinical specimens were measured using the QIAcuity One dPCR system (Qiagen). The reactions were set up using the QIAcuity OneStep Advanced Probe Kit (Qiagen), influenza A virus-specific primers and probes [119], and nucleic acids freshly extracted using the MagMAX™ Pathogen RNA/DNA Kit (Applied Biosystems), following manufacturers' instructions. After reactions were distributed into QIAcuity 26k Nanoplates (Qiagen), the plates were incubated at 50°C for 40 min, followed by 95°C for 2 min and 45 cycles of 95°C for 5 sec and 55°C for 30 sec. The QIAcuity One instrument imaged the nanoplates after thermocycling completed and calculated RNA copy numbers in the reaction based on the number of positive partitions, which were back calculated to RNA copies/mL in the original sample. Multiple dilutions of the extracted nucleic acid were included to ensure at least one falls within the dynamic range of the dPCR assay.

Results

Efficient discretization and uniform flow are enabled by the dFA chip design

The dFA chips were fabricated using two layers of polydimethylsiloxane (PDMS) patterned by soft lithography [120] and bonded together to form an enclosed microwell array and fluidic channel for cell, sample, and reagent delivery. Each chip contained a

13x13 array of square wells with 200 μm width, 120 μm depth, and 50 μm spacing between adjacent wells (Fig. 2.3). The enclosing channel, centered around the array, had a height of 120 μm spanning 38 mm in length and 11 mm in width. The selection of PDMS as the chip substrate material was motivated by the high gas permeability [120], excellent biocompatibility [121–123], and low toxicity [121,123] of PDMS, making it a suitable material to support on-chip cell culture. The high optical transparency [120,123] and low auto-fluorescence [124] of PDMS also ensures efficient assay readout from the fabricated devices. However, because PDMS is a hydrophobic material, the chips required hydrophilic surface modification to enable effective well filling, discretization, and cell attachment. While PDMS can be temporarily rendered hydrophilic by oxygen plasma treatment [125,126], the modified surfaces quickly revert to their native hydrophobic state. Thus, to provide a more robust hydrophilic modification, an embedded Pluronic block copolymer strategy [117,127] was utilized. By mixing Pluronic surfactant with PDMS prepolymer during dFA chip fabrication, surfactant molecules at the PDMS surface tend to expose their hydrophilic chain segments while embedding their hydrophobic segments within the PDMS bulk, as summarized in Fig. 2.4. When attempting to discretize culture media in dFA chips fabricated from native PDMS without the addition of Pluronic, the substrate surface energy was insufficient to prevent the oil phase from lubricating the PDMS surface, resulting in droplet formation and removal of media from the wells. In contrast, when combined with oxygen plasma activation to promote bonding of the PDMS layers during chip fabrication, the Pluronic-modified chips yielded consistent and complete retention of culture media within the microwells when flowing oil in the enclosing channel to discretize the wells.

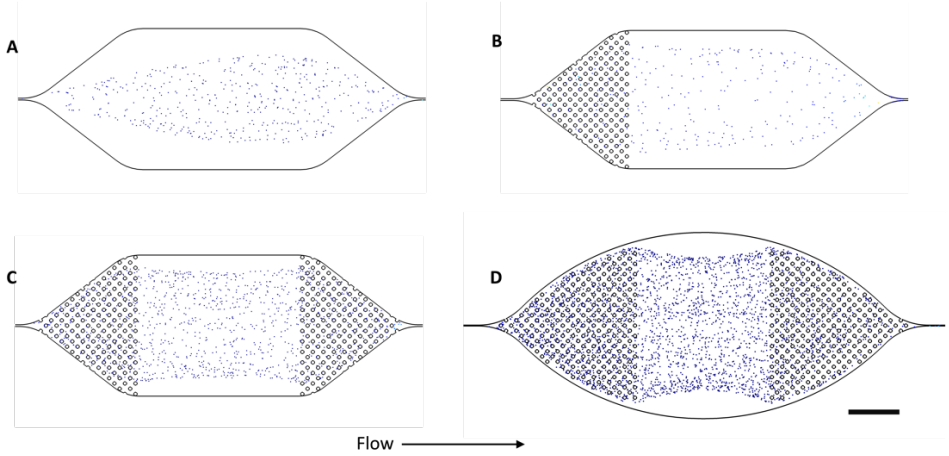


Figure 2.7. Cell suspension flow simulation results. COMSOL Multiphysics simulation depicting the flow behavior of cell suspension liquids through (A) a rectangular enclosing channel without pillar arrays, (B) a rectangular enclosing channel with pillar arrays on the inlet, (C) a rectangular enclosing channel with pillar arrays on both the inlet and the outlet, and (D) a continuously curving channel with pillar arrays on both the inlet and the outlet, designed to promote mixing and uniform lateral distribution of the cells to the microwell arrays. Scale bar: 3 mm.

The dFA chips were designed with square arrays of 169 identical microwells residing within an open chamber aligned to the wells through the use of the multilayer mold fabrication process. While early chips were fabricated by manually aligning and bonding two patterned layers of PDMS, one containing the microwells and the other containing the channel structure, the final self-alignment process was found to prevent asymmetry within the flow field and avoid maldistribution of cells across the microwell array (data not shown here). To further improve the seeding uniformity across the array, COMSOL Multiphysics simulations of the flow of cell suspensions through various channel geometries and mixing structures were performed. These simulations (Fig. 2.7) revealed that the cylindrical pillar array serves to disrupt the initial streamlines in the upstream cell delivery channel, thereby improving the lateral dispersion of cells within the chamber. Similarly, chambers with symmetric pillar arrays at the inlet and outlet,

together with designs employing a constant wall curvature, were also found to enhance seeding uniformity within the array. Each of these modifications was validated experimentally before selecting the chip design featuring a pair of micropillar arrays located at the inlet and outlet of the chamber (Fig. 2.7.D), for all further experiments. In the absence of these pillars, cells were observed to preferentially flow along the centerline of the channel, leading to lower cell seeding density within microwells located farther from the centerline (data not shown here).

MDCK cells form confluent, isolated monolayers within the dFA platform

To next prepare the chip for virus introduction, a suspension of MDCK cells was perfused into the chip (Fig. 2.5.A) to fill the microwell array chamber, after which the flow was halted and cells were allowed to sediment into the microwells and adhere to the well surfaces. Notably, the combined Pluronic and oxygen-plasma based hydrophilic modification of the PDMS surface was found to be effective in promoting cell adhesion, eliminating the need for complicated patterning and coating of extracellular matrix protein like collagen and fibronectin to support microwell culture.

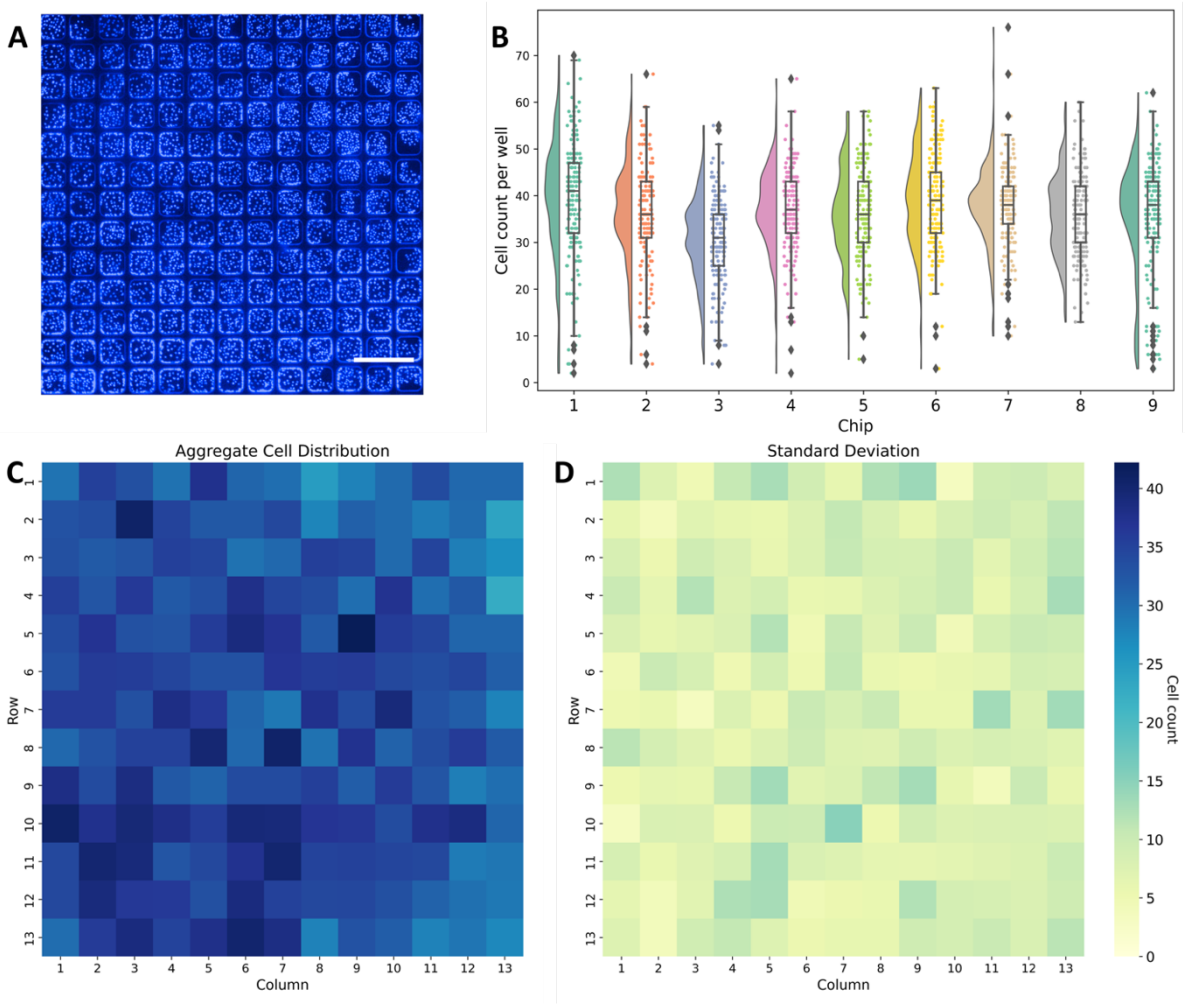


Figure 2.8. Distribution of MDCK cells. (A) Sample image displaying typical MDCK cell distribution across the 13x13 microwell array following cell seeding, expansion, and nuclear staining for visualization. Scale bar: 500 µm. (B) Distributions of cells within 9 individual chips. (C) Mean and (D) standard deviation for aggregate cell distributions within each array position across all 9 chips used for the digital focus assay with MM overlay.

The lateral well dimensions were selected to support approximately 30-50 MDCK cells within each well at confluence, and the well height was designed to ensure robust discretization while also trapping a sufficient volume of culture medium (4.8 nL) to maintain high cell viability during assay operation. Indeed, following overnight incubation, nearly confluent cell monolayers were achieved within the individual microwells (Fig. 2.5.B; 2.8.A). The distributions of cells for all 9 chips used for

evaluation of the digital focus assay are displayed in Fig. 2.8.B. As expected, most microwells contained between 30 and 50 cells 24 h after seeding. Specifically, 67.5% of the total microwells across the 9 chips contained between 30 and 50 cells while 84% of the microwells contained between 25 and 55 cells each. To better visualize the spatial distribution of the cells across the microwells, a heatmap of the distribution of cells per microwell in the 13x13 array averaged across all 9 chips along with the corresponding standard deviation of the distribution are presented in Fig. 2.8.C and 2.8.D.

While any cells initially seeded onto the upper plateau of the microwell chip were found to be efficiently removed by shear forces during the flow of overlay media into the chip (data not shown here), the hydrophilic surface modifications employed during device fabrication to promote effective microwell filling and cell attachment can potentially support migration of cells from the wells and onto the plateau following well discretization, leading to unwanted bridging of cells between adjacent wells during longer term culture. Bridging can potentially allow the contents of discretized microwells to enter neighboring wells, resulting in virus cross-contamination that may comprise assay accuracy. To quantify cell bridging experimentally, the bridging probability was defined as the total number of bridging events observed scaled by the total number of well gaps across which bridging may occur within a single array, with results calculated for assays performed with either MCC or MM overlays. As seen in Fig. 2.9, the average bridging probability is below 1% for chips prepared with MCC overlay regardless of the culture time, while chips prepared with MM overlay exhibited

significantly higher bridging at 8 h compared with 24 h. For both overlays, bridging at 24 h was found to be negligible.

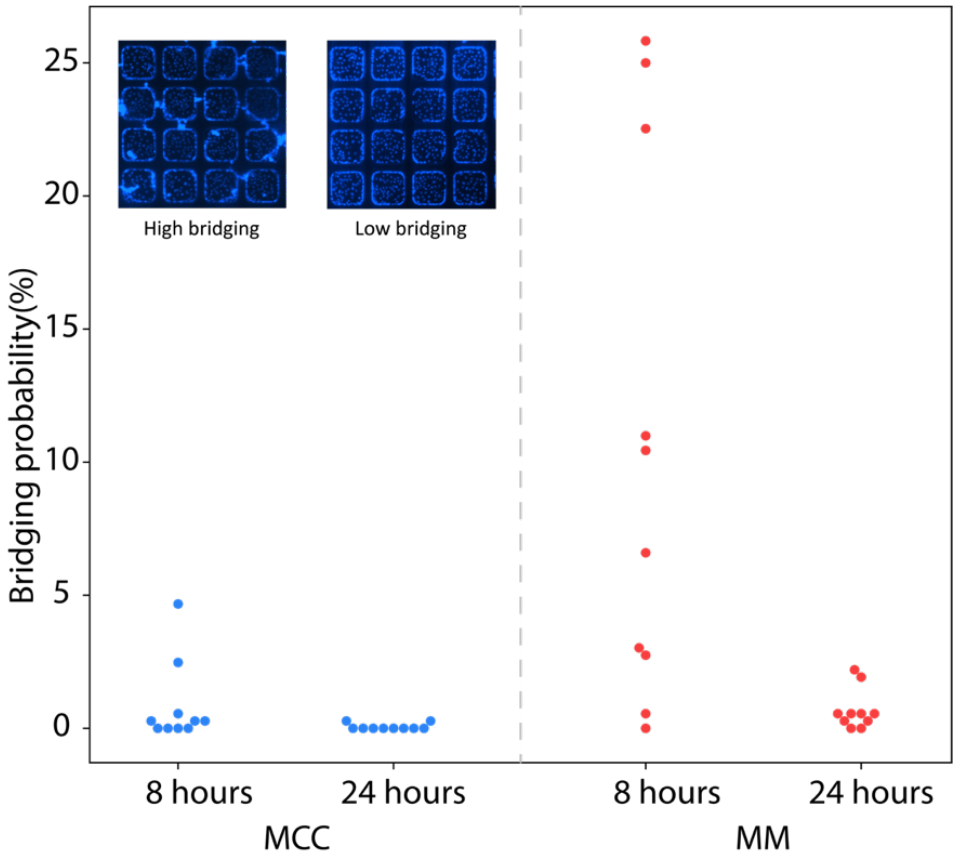


Figure 2.9. Impact of overlay medium on cell bridging across microwells. Quantification of cell bridging events between adjacent microwells for MCC and MM overlays at 8 h and 24 h time points. Bridging probability is defined as number of bridging events observed scaled by the total number of adjacent well gaps across which bridging may occur within a single array (n=10 chips for each overlay). Insets of high and low bridging example cases are included.

Infectious influenza A virus titers can be determined using the dFA platform

Following cell seeding, serial dilutions of an influenza A virus inoculum was then introduced into chips in parallel and incubated for 2 h to allow virus within the upper chamber to diffuse into the microwells for uptake by the MDCK cells (Fig. 2.5.C).

Residual virus was next removed from the system by flowing overlay media through the chip (Fig. 2.5.D), followed by injection of mineral oil to discretize the wells (Fig. 2.5.E). The chip was then incubated to achieve a total inoculation time of up to 24 h (Fig. 2.5.F), including the initial incubation step.

To image the resulting distribution of microwells containing infected cells, the oil and overlay media were flushed out with PBS to allow the introduction of reagents for fixing and permeabilizing the cells (Fig. 2.5.G), and for immunofluorescence detection of influenza nucleoprotein within the wells (Fig. 2.5.H and 2.5.I). The flow-through architecture of the dFA chips allowed all fluid handling steps involved in fixing and staining the cells to be efficiently performed by manually swapping syringes containing different reagent solutions between each step, using a single syringe pump to control all injections with predictable and repeatable performance.

Fluorescence microscopy images of the 13x13 array with the MDCK cells stained for influenza A virus nucleoprotein were captured for all dilution factors. Image analysis was automated through a Python script designed to generate a binary map of infections across the array. The raw fluorescence images together with the mapping of positive wells at each dilution are presented in Fig. 2.10.A.

The distribution of the finite number of infectious virions in the sample among the microwells and the resulting infections can be approximated as a Poisson distribution, with the probability of n virions residing within a particular microwell given by [128],

$$p(n) = \frac{\lambda^n e^{-\lambda}}{n!} \quad (2.1)$$

where λ is the mean number of virions per microwell across the full array. Taking the case of n = 0, the probability of zero virions appearing in a particular microwell is given by,

$$p(0) = e^{-\lambda} \quad (2.2)$$

such that,

$$\lambda = -\ln(p(0)) \quad (2.3)$$

or equivalently,

$$\lambda = -\ln(1 - \hat{p}) \quad (2.4)$$

where $\hat{p}$ is the probability of a well containing at least one virus particle. Since the mean count of virions per microwell is simply the product of the virus concentration (c) and microwell volume (V), the viral titer of an unknown sample can be determined from Eqns. (2.1) and (2.4) as,

$$c = -\frac{\ln(1-\hat{p})}{V} \quad (2.5)$$

The viral titer can be found from Eqn. (2.5) by counting the number of wells positive for viral antigen, which is equivalent to the value of $\hat{p}$ under the assumption that a single virion is capable of infecting a target cell and leading to replication within the well. Note that the effective well volume is the volume of sample from which virions are free to infect the MDCK cells during the initial inoculation event. To account for virus that can diffuse into the wells from the sample delivery channel, the effective well volume was calculated as the sum of the geometric volume of the microwell and the volume of the column in the enclosing channel directly over the microwell, assuming that the initial volume of culture media within each well is fully replaced by virus suspension during sample perfusion. Since the channel height is the same as the microwell depth, the effective volume of virus sample delivered to each well is twice the geometric well volume, and is calculated to be V = 9.6 nL.

Unlike a conventional focus assay, in which individual foci are counted, the digital assay introduces uncertainty in the quantification process due to statistical variability in virus distribution. The confidence interval for the predicted value of $\hat{p}$ can be approximated for large values of n by[129]:

$$\hat{p}_{low,high} = \hat{p} \pm \alpha\sqrt{\frac{\hat{p}(1-\hat{p})}{n}} \qquad (2.6)$$

where α = 1.96 for a 95% confidence interval. The lower and upper limits for the confidence interval of the viral titer can then be found by employing the values of $\hat{p}_{low}$ *and* $\hat{p}_{high}$ in Eqn. (2.5).

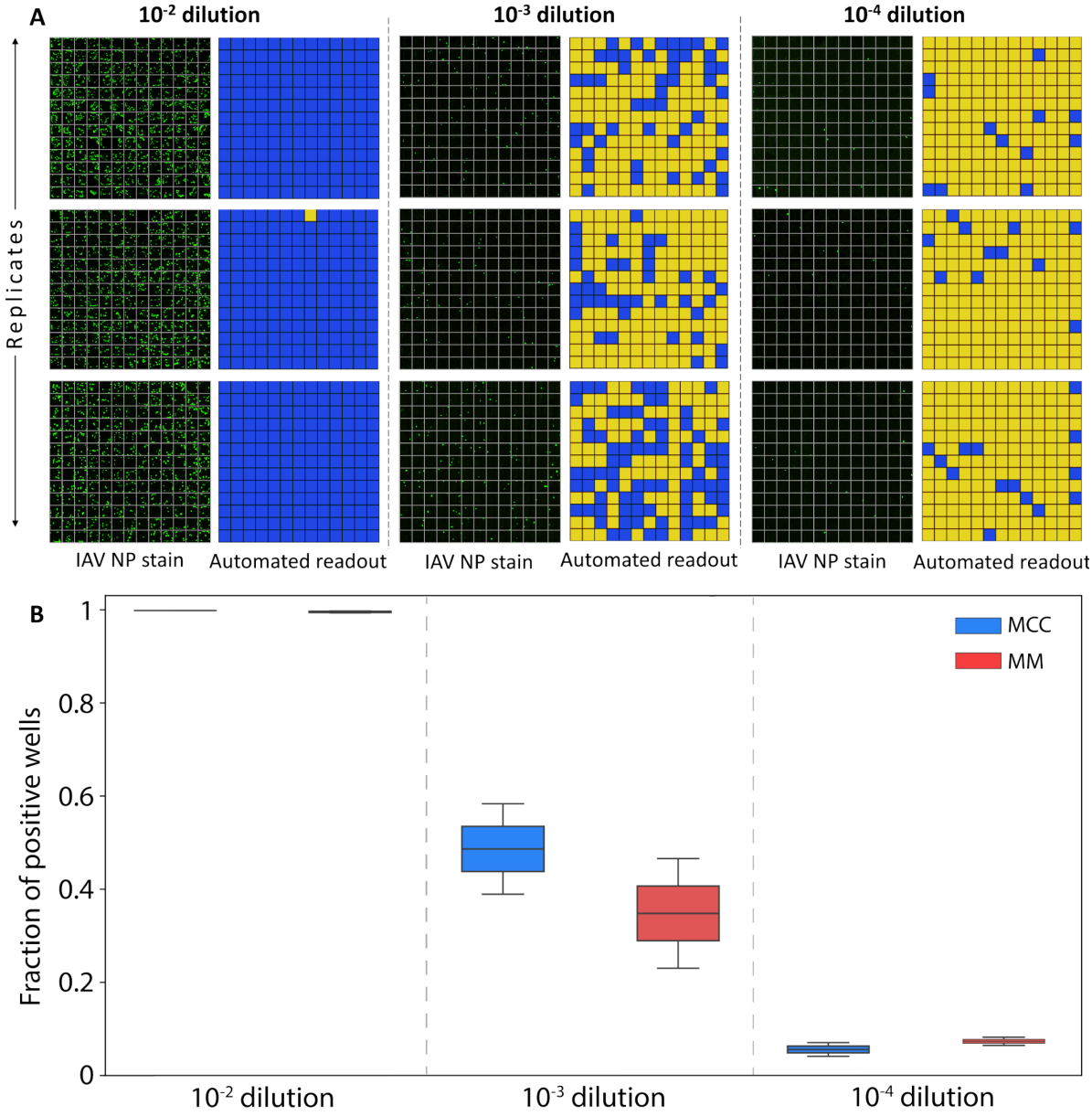


Figure 2.10. Digital assay readout. (A) Paired images of Influenza A virus nucleoprotein stain and resulting binary readouts (blue = positive, yellow = negative) generated by automated image processing at increasing virus stock dilution factors of 10^{-2}, 10^{-3} and 10^{-4} (MM overlay, 3 replicates for each case shown). (B) Microwell fractions exhibiting positive infection using MCC and MM overlays for each viral stock dilution (n=3 for each case). The error bars in the boxplots represent the variation in data between the replicate chips at each condition, with the box bounding the data between the first and third quartiles, while the whiskers on either end span 1.5 times the interquartile range.

For each experiment, the value of $\hat{p}$ was determined as the fraction of positive wells in the binary readout. Identical experiments were performed using both MCC and MM overlay media at each various dilution factor to evaluate the impact of the overlay on assay performance. The resulting viral titers and confidence limits were calculated using Eqns. (2.5) and (2.6), with results presented in Table 2.1 and Fig. 2.10.B.

Table 2.1. Comparison of viral titers measured by dFA and plaque assay. Mean viral titers from dFA for various overlays and dilutions of the viral inoculum with a matching plaque assay. The mean positive well fraction, the mean viral titer and the associated confidence intervals for the dFA were obtained by aggregating data from the three replicates at each combination of overlay and dilution.

Assay format:	**Digital Focus Assay**						**Plaque Assay**
Dilution factor:	10^{-2}		10^{-3}		10^{-4}		10^{-6}
Overlay:	MCC	MM	MCC	MM	MCC	MM	Agar
Mean positive well fraction ($\hat{p}$):	1.00	0.998	0.414	0.331	0.051	0.073	-
Mean viral titer (PFU/mL):	-	-	5.9×10^7	4.4×10^7	5.5×10^7	7.9×10^7	5.6×10^7
95% confidence interval:	-	-	4.8-6.4x10^7	3.6-4.8x10^7	3.4-7.6x10^7	5.4-10.5x10^7	-

At the lowest dilution factor of 10^{-2}, the high virus concentration was sufficient to yield infected cells in all microwells for the majority of replicates, preventing the viral titer

from being determined using Poisson statistics. At dilution factors of both 10^{-3} and 10^{-4}, positive well fractions were within a range that enabled virus concentration to be estimated (Fig. 2.11). Good agreement was found between the resulting values and the reference titer determined through a plaque assay, with average titer predicted from all assays falling within 10% of the reference value. Pairwise t-tests comparing viral titers from the dFA and plaque assay, assuming normality, yielded p-values ranging from 0.20 to 0.95. This lack of statistically significant difference supports strong agreement between the two methods. This supports strong agreement between the two quantification methods. Further, no clear difference was observed between assays utilizing either MCC or MM overlays.

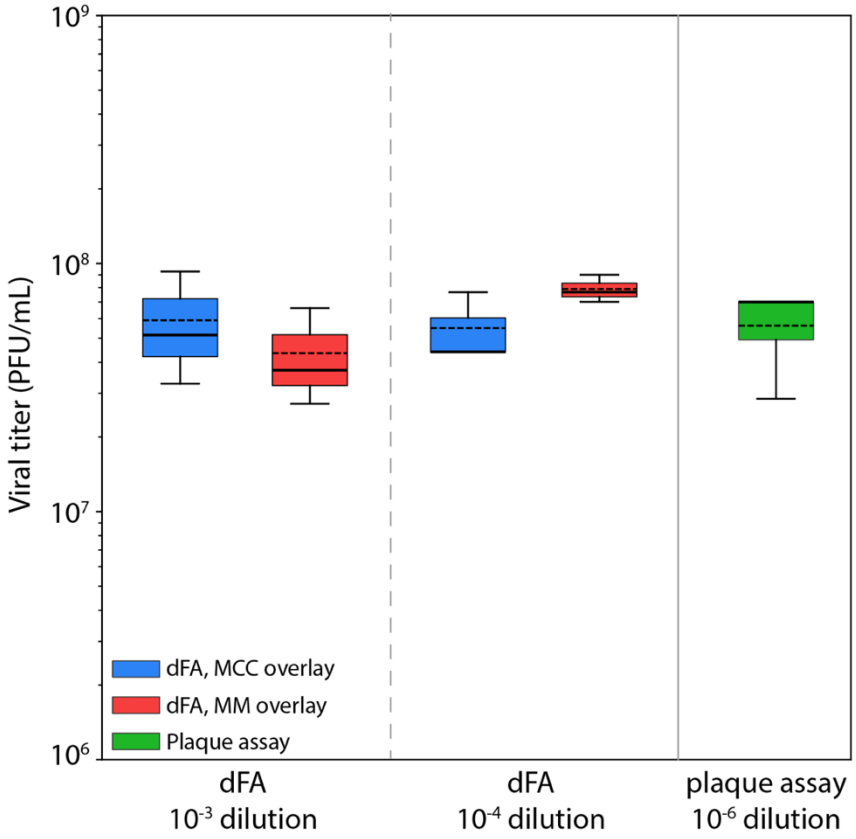


Figure 2.11. Viral titers determined from dFA and plaque assay. Measured viral titers determined by the digital focus assay when utilizing different initial dilution factors. Assay results are presented for both MCC and MM overlays, and compared with the readout from a plaque assay for the same viral stock. The error bars in the boxplots represent the variation in data between the replicate assays at each condition (n=3), with the box bounding the data between the first and third quartiles, while end whiskers span 1.5 times the interquartile range. Solid and dashed lines represent median and mean viral titers, respectively. A Z-test was applied to compare each dFA distributions against the reference plaque assay, yielding Z-scores between 0.07-1.5.

The dFA platform is compatible with clinical specimens

Following validation with model H3N2 virus, the dFA platform was evaluated using clinical specimens collected as part of an ongoing influenza transmission study. Samples were collected from a single donor on two subsequent days for characterization by dFA. Aliquots of each sample were also reserved for matching dPCR analysis. A summary of results is presented in Table 2.2. The first specimen

collected on the day of admission into the study exhibited nearly 100% average positive well counts from all three dFA replicates. This result corresponds to a minimum titer of $5.9x10^5$ PFU/mL, but does not allow an upper bound for the titer to be specified. The second specimen collected on the subsequent day yielded an average positive well count of 67.7%, resulting in a predicted viral titer of $1.3x10^5$ PFU/mL. Quantification by dPCR indicated that these specimens contained $3.9x10^8$ and $1.3x10^7$ influenza A virus RNA copies/mL, respectively.

Discussion

The initial direction for developing a microfluidic cell culture platform for quantifying viable viruses centered on adapting the plaque assay, given its status as the gold standard for infectivity measurements and its relatively low cost. However, several practical considerations ultimately motivated a shift toward digital focus assays. Plaque assays require extended incubation periods to detect cytopathic effects, as host cell death typically occurs several days after viral infection. For influenza virus, this process can take approximately five days following initial inoculation. While long-term culture is not problematic in conventional plate-based assays, it presents substantial challenges in microfluidic microwell formats. The limited volume of individual microwells constrains the supply of fresh nutrients and accelerates the accumulation of metabolic waste, restricting the ability to sustain viable cell culture over multiple days. As a result, prolonged incubations introduce ambiguity, as cell death may stem from compromised culture conditions rather than viral infection, confounding interpretation of results.

In contrast, focus assays are more compatible with microfluidic discretization. Because they rely on immunostaining of viral proteins rather than cytopathic effect, infections

can be detected within 24 hours, a timeframe that is well supported by the nutrient and waste-handling capacity of microwell volumes. This approach minimizes culture-related artifacts and enables more reliable quantification of viable viruses. Moreover, focus assays offer broader applicability, not all viruses form plaques or induce visible cytotoxicity, whereas focus assays can detect infection regardless of cytopathic outcome. Although focus assays traditionally require antibodies making them more expensive, microfluidic miniaturization reduces reagent consumption significantly, making it more cost-effective.

The dFA offers several advantages to other conventional assays. The microfluidic architecture of the device, for example, serves to simplify assay implementation, while the small volume of the combined microwell array and fluid delivery channel (approximately 30 μL) minimizes the quantities of sample and reagents required for assay operation. In practice, multiple chips can be run in parallel, allowing the number of microwells to be increased without redesigning the device, or the microwell design can alternately be modified to increase the array density to improve readout confidence with only a minor increase in reagent consumption.

Reliable digital readout from the dFA requires that cells do not grow or migrate beyond the confines of their original wells, which would result in transfer of virus between adjacent wells. Assays performed using MCC overlays were seen to exhibit lower levels of cell migration and well bridging during the early stages of culture compared with MM overlays, presumably due to the higher viscosity of the MCC media limiting

cell mobility. However, minimal bridging was observed for both MCC and MM overlays at 24 h, revealing that both types of media are effective at preventing the migration of infected cells between adjacent microwells over relevant assay time scales. The significant decrease in bridging probability at 24 h is believed to be due to extended exposure of the cells in the plateau region to mineral oil, thereby reducing survival of these cells.

A potential advantage of the dFA compared to traditional focus assays is improved flexibility in assay endpoint time. Regardless of assay implementation, short culture times that do not allow for sufficient virus replication will result in foci comprised of single infected cells, making it difficult to distinguish virus expansion from other visual artifacts, or cells with insufficient virus expansion to allow for effective staining [76,77], making the readout unreliable. As a result, the lower limit on assay time is dictated by virus expansion kinetics. On the other hand, at long endpoint times excessive proliferation of progeny virus risks readout inaccuracy due to the merging of neighboring foci, thus requiring that focus assay times be optimized for specific viruses, cells, and culture conditions. In contrast, because the dFA maintains physical isolation of culture volumes to prevent crosstalk between the microwells, readout integrity is not compromised by excessive proliferation of virus within the discretized wells. To evaluate the impact of extended culture time on assay performance, experiments were performed with incubation periods ranging from 18 h to 48 h post infection. For the MDCK cells and influenza virus used in this dissertation, incubation

periods longer than 30 h were observed to result in increased bridging of cells between adjacent microwell volumes, defining an upper limit for dFA endpoint time.

The dFA platform also simplifies the process of assay readout. In a traditional FFA, large areas within each well of a 24 or 96 well plate must be manually scanned under a microscope, a laborious process that can introduce subjectivity in quantification. Automated foci counting is possible with specialized instruments, but these tools are cost prohibitive for many end users. In contrast, the dFA only requires imaging across the small microwell array area, with a binary readout that supports robust automation through simple image processing code without the need to determine the precise number of infection events within each well.

While the chip design was optimized to reduce variability in cell seeding density, differences in the number of cells initially delivered to each microwell should not significant affect assay readout. In our experiments, between 30 and 50 cells were typically observed in each microwell following the overnight cell expansion step, providing sufficient cell density to allow infectious virus to diffuse to at least one cell during the initial 2-hour incubation window, noting that the diffusion time scale for influenza virus in a 200 μm microwell is calculated from the Stokes-Einstein equation to be approximately 75 min. For microwells exhibiting either limited cell expansion or cell loss during reagent perfusion, the selected wells may simply be omitted from analysis to prevent bias in the digital quantification process.

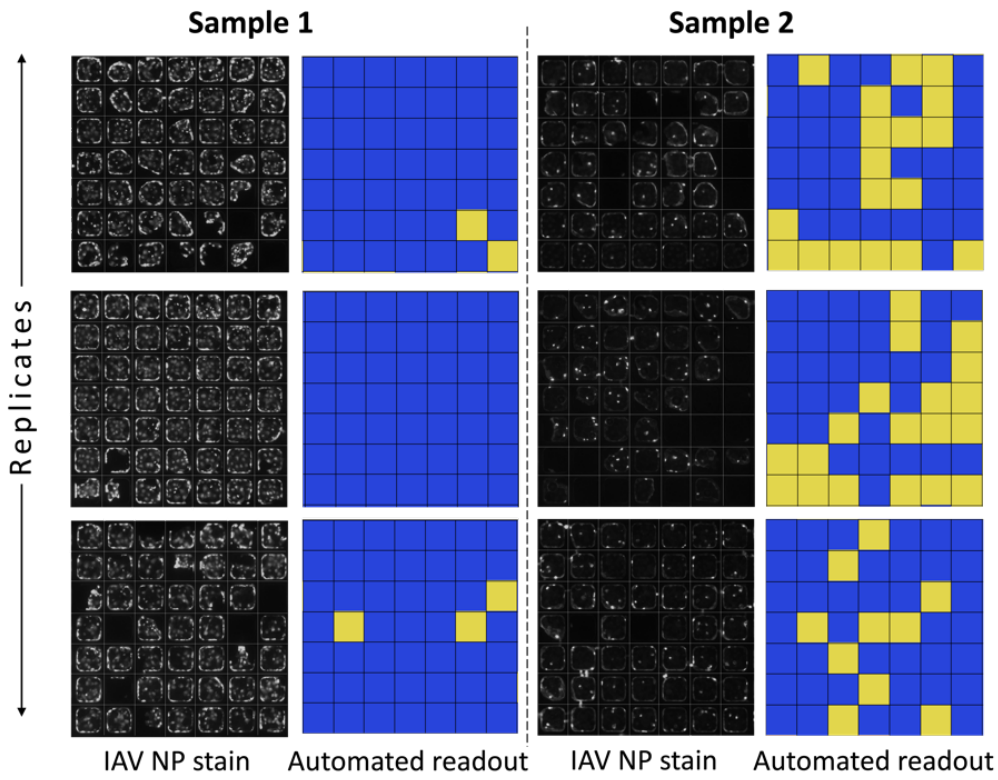


Figure 2.12. Fluorescence images and automated dFA readout for nasal swab specimens. Images and binary readout for a subset of wells in each of 3 replicate chips run on nasal swab specimens with high (sample 1) and low (sample 2) viral titer. Both samples were evaluated without dilution.

Assay results for the nasal swab samples (Fig. 2.12) demonstrate that the dFA can successfully be applied to clinical specimens containing contemporary influenza strains. Because large variability in viral load is commonly seen for influenza samples collected by midturbinate swab, with concentrations ranging from approximately 10^3-10^8 copies/mL [130], clinical samples should ideally be characterized at multiple dilutions to ensure that at least one concentration level lies within the dynamic range of the assay. Unfortunately, the low sample volumes available for our clinical specimens did not allow for the assay to be run at multiple dilution levels to establish optimal dilutions for quantification of infectious virus within each sample. As a result, the high titer

observed for the first sample, which was found to be above the dFA upper limit of detection (approximately $6x10^5$ PFU/mL for the selected dilution), prohibited quantitative comparison between the assays. Regardless, consistent quantitative results were seen across all replicates for the lower titer sample, with predicted titers well within the dFA dynamic range. Furthermore, a positive correlation between measured titers and RNA copy numbers for both clinical specimens was observed.

Table 2.2. Summary of assay results for nasal swab specimens. Measured average positive well fractions and calculated assay titers using dFA chips (n=3 for each sample), together with corresponding viral RNA concentrations measured by dPCR.

Specimen number:	1	2
Positive well fraction ($\hat{p}$)	0.970	0.677
Calculated titer (PFU/mL)	$>5.9x10^5$	$1.2x10^5$
dPCR results (RNA copies/mL)	$3.9x10^8$	$1.3x10^7$

In its current implementation, the tubing connecting the syringe pump to the chip introduces significant dead volume, resulting in unnecessary reagent waste. For the experiments described here, the dead volume associated with the inlet tubing was approximately 3x higher than the full on-chip volume. Modifying the apparatus to employ pneumatic pressure rather than displacement-based pumping for flow control may further reduce reagent waste, allowing reagents to be directly pipetted into the chip inlet port prior to pneumatic injection into the microwell array, thereby eliminating the need for added tubing.

In a kit designed to be shared with other laboratories for quantifying viable viruses using the dFA, the following components would be required. To enable dissemination of the dFA technology, the kit would need to include both physical and digital components, along with initial training for end users. A brief training session would be important for familiarizing users with key assay steps, including optimal cell seeding, oil-based droplet discretization, reagent handling, and chip imaging after immunostaining.

On the physical side, the kit should provide redesigned microfluidic chips. In their current form, the devices rely on syringe pump-based infusion, which can pose challenges for untrained users. Redesigning the chips to allow simple pipetting of reagents would significantly improve accessibility and reproducibility in external laboratories. In addition to hardware, the kit should include updated software tools. The current Python-based image analysis script requires users to manually input the coordinates of the first microwell. A more robust version of the script capable of automatically detecting microwell positions, regardless of microscope or camera setup, would greatly simplify analysis and broaden the applicability of the assay across diverse laboratory environments.

Together, the combination of redesigned chips, improved software, clear documentation, and targeted training would create a self-contained dFA kit that facilitates adoption by new users while minimizing the technical barriers associated with microfluidic discretization and digital quantification workflows.

With its low sample and reagent volume requirements, simple assay implementation, and flexible endpoint timing, together with its small form factor, scalable format, and compatibility with any suitable fluorescence microscope for assay readout, the dFA technology is a cost-effective and accessible alternative to traditional focus assays that can also be adapted for use with other adherent cell lines and pathogens, making it a promising platform for a range of infectious disease research and diagnostic applications.

Acknowledgements

This chapter is adapted in part from Siddharth Raghu Srimathi et al., *Microfluidic digital focus assays for the quantification of infectious influenza virus*, Lab on a Chip, 2025, **25**, 2004 **DOI:** 10.1039/D4LC00940A.

I gratefully acknowledge the contributions of Maxinne A. Ignacio, Maria Rife, Sheldon Tai, Donald K. Milton, Margaret A. Scull, and Don L. DeVoe to the experimental design, data collection, resources, and manuscript preparation of this work.

Chapter 3: Microfluidic discretization for single-particle analysis of aerosol emulsions

Understanding how pathogens are distributed among individual aerosol particles is critical to advancing models of airborne transmission and improving control strategies. Single-particle analysis can reveal whether infectious agents are uniformly dispersed across droplets or concentrated in a subset, which directly informs estimates of the quanta of infection and the relative contribution of different particle fractions to transmission. Conventional bulk assays measure overall viral concentration but inherently homogenize aerosol samples in collection media, obscuring particle-to-particle variability and preventing correlation of pathogen presence or infectivity with droplet size or composition. Size-fractionating samplers such as impactors and cyclones can separate aerosols by aerodynamic diameter, yet each fraction is still homogenized, so single-particle distributions remain unresolved.

This chapter outlines an alternative approach that couples controlled collection of aerosols as discrete aqueous droplets in oil with microfluidic manipulation. Specifically, condensation growth tube (CGT)-based emulsion collection is paired with a droplet-merging platform so that individual droplets or small sets of droplets can be brought into contact with assay reagents in a defined manner. This enables targeted interrogation of viral components or infectivity at near single-particle resolution and provides a framework for compositional analysis that preserves droplet-level heterogeneity. The sections that follow present preliminary aerosol-collection studies

and demonstrate the droplet-merging workflow to assess feasibility and practical considerations for bioaerosol analysis.

Experimental

Aerosol collection as emulsions using CGT

Preliminary experiments were performed to collect aerosols as emulsions using the BioSpot-VIVAS, a condensation growth tube (CGT) system designed and developed by Aerosol Dynamics Inc. The system samples particles directly from the ambient environment without upstream impactors, operating at a flow rate of 8 L/min, and was installed at the University of Maryland Laurel Medical Center. The system consists of three thermal conditioning zones: a Conditioner stage maintained at 5 °C to pre-cool and humidify the incoming air, an Initiator stage heated to 45 °C to induce water vapor supersaturation and particle growth via condensation, and a Moderator stage at 12 °C to stabilize the grown droplets before collection. At the sample collection port, a 35 mm Petri dish containing 2 mL of mineral oil supplemented with 5% (v/v) surfactants (Span 80 and Tween 80) was placed.

Preliminary sampling experiments were conducted with collection durations of 60 minutes and 90 minutes. Immediately after collection, the samples were transferred into vials and transported back to the University of Maryland, College Park. Aliquots of 5 µL from each sample were dispensed onto glass slides and imaged using a microscope.

The images were then imported into ImageJ for analysis to determine the droplet size distribution.

Microfluidic droplet generation

While aerosols can be collected as emulsions using CGTs, achieving robust and reliable collection requires extensive optimization. Moreover, for developing the downstream technology to analyze emulsions, the specific method of emulsion creation is less critical. Consequently, synthetic model emulsions generated using microfluidics serve as a practical alternative. Using the aforementioned planar flow-focusing droplet generators, droplet size is determined primarily by the viscosity of the continuous phase and the interfacial energy, scaling with the Capillary number (Ca), a dimensionless number representing the ratio of viscous to surface tension forces, as $d \propto Ca^{-1/3}$. The viscosities of the phases are intrinsic material properties and cannot be altered significantly, although higher viscosity oils can help produce smaller droplets. Interfacial energy, however, can be reduced substantially by adding surfactants to the continuous oil phase, providing an additional means of controlling droplet size. Higher surfactant concentrations can also enhance droplet stability in the emulsion through steric or electrostatic interactions, as well as by inhibiting Ostwald ripening.[131]

The planar flow-focusing devices were fabricated using soft lithography with single-layered photoresist molds, as previously described in Chapter 2. Briefly, a 15 μm layer of SU-8 2015 was spin-coated onto a 4″ silicon wafer. The coated wafer was soft-baked according to the manufacturer's instructions, and the designs for the planar flow-

focusing devices were exposed using a maskless aligner. Following a post-exposure bake, the unexposed regions of the coated wafer were developed away using SU-8 developer (Kayaku Advanced Materials), leaving behind the patterned wafer. The wafer was then hard-baked at 150 °C for 30 minutes to complete mold fabrication. Fig 3.1 shows the fabricated SU-8 molds, which were inspected with an optical profilometer to verify that they met the design specifications.

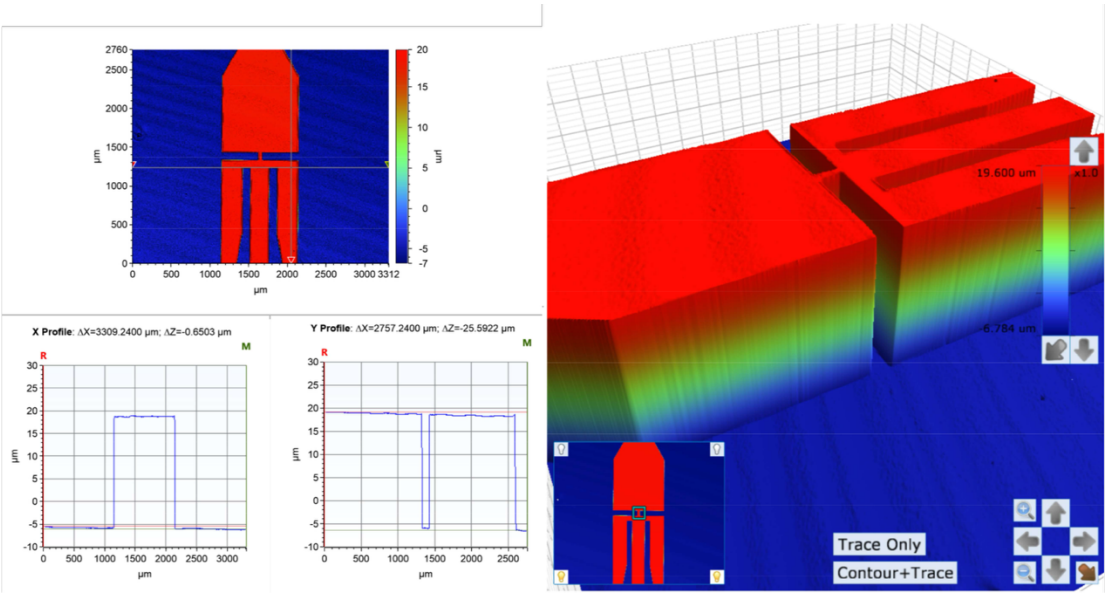


Figure 3.1. Measurement of the SU-8 mold for the planar flow-focusing droplet generators using an optical profilometer, showing a feature height of 25 µm, the x- and y-profiles, and a 3D contour model of a single device.

Soft lithography was performed by pouring PDMS mixed with crosslinker at a 10:1 ratio onto the SU-8 mold and curing at 80 °C for 3 hours. After curing, the PDMS layer was peeled from the mold, and individual blocks containing 3-4 devices were cut. Holes were punched for fluidic access, and the devices were directly bonded onto 1″ x 3″ glass slides (AmScope) with the feature side facing the glass, using oxygen plasma activation. 24-gauge blunt-tip needle segments (CML Supply) were inserted into the

fluidic access holes to connect flexible Tygon tubing (0.020″ ID x 0.060″ OD, Masterflex), interfacing the chip with syringe pumps for the water phase (PHD 2000, Harvard Apparatus) and the oil phase (Fusion 400, Chemyx).

Another parameter influencing droplet size in planar flow-focusing devices is the device geometry, including the widths of the three channels, the orifice width, the distance from the channel junctions to the orifice, the downstream channel width, and the channel height.[105] While variations in all of these parameters affect droplet size, as observed experimentally in this study, the geometric factor with the greatest influence is the hydraulic diameter of the orifice, which depends on the orifice width and the channel height. Devices with a 30 μm orifice and a 25 μm channel height, giving a hydraulic diameter of 27.3 μm, were used to reliably produce monodisperse water droplets with diameters between 15 and 20 μm in mineral oil. The droplet generation process reached steady state within approximately 10 minutes and remained remarkably stable, producing monodisperse emulsions for up to 48 hours. Smaller orifice widths were successfully fabricated and produced smaller droplets, however, these were highly susceptible to clogging and disruption due to microscopic impurities in either phase, which could cause partial or complete occlusion of the orifice. As a result, the 30 μm orifice was preferred for applications requiring high-throughput droplet generation over extended periods, despite the inability to reliably produce droplets smaller than 15 μm. Fig. 3.2 shows monodisperse droplets of 12.5 μm and 18 μm produced using planar flow-focusing devices with orifice widths of 15 μm and 30 μm, respectively.

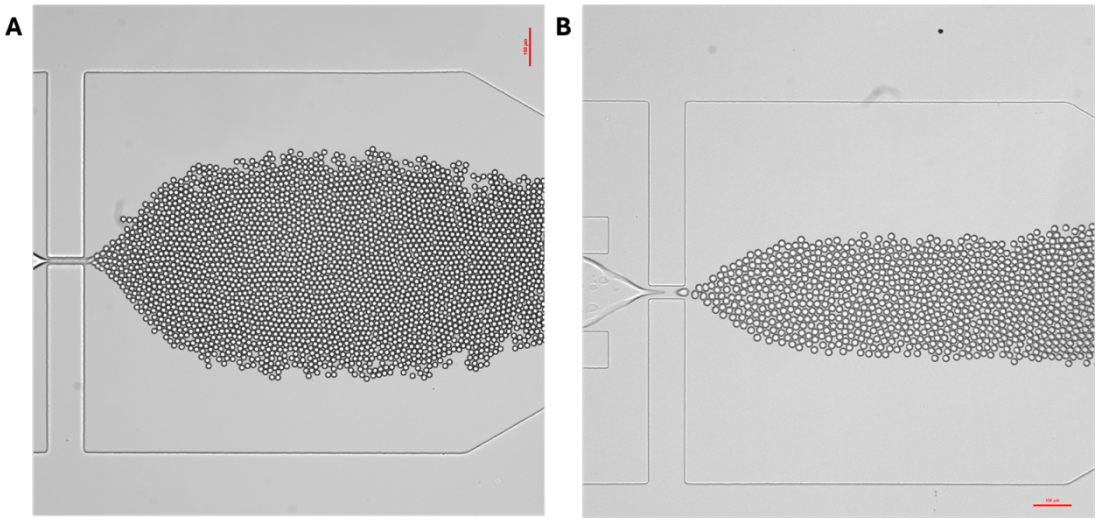


Figure 3.2. Microfluidic planar flow-focusing droplet generators: (A) 15 µm-orifice devices generating monodisperse emulsions with a mean droplet diameter of 12.5 µm; (B) 30 µm-orifice devices generating monodisperse emulsions with a mean droplet diameter of 18 µm, shown 24 hours after the start of droplet production.

To produce the monodisperse 18 µm droplets used in this work, the oil phase flow rate was set to 0.54 µL/min and the aqueous phase flow rate to 0.18 µL/min, yielding a water-to-oil flow rate ratio of 1:3 and a droplet production rate of approximately 1000 Hz. For model viral emulsions, the aqueous phase contained influenza A virus A/Puerto Rico/8/1934 (H1N1), commonly referred to as PR8, at a concentration of 5E4 FFU/mL, and was emulsified into water-in-oil droplets using the planar flow-focusing droplet generator for this study.

For optimal stability of water-in-mineral oil emulsions, the surfactant mixture should have a hydrophilic-lipophilic balance (HLB) of approximately 6 and a total surfactant concentration exceeding 5% (v/v).[132] Span 80, a commonly used lipophilic surfactant

for stabilizing water-in-oil emulsions, has an HLB of 4.3. To achieve the desired HLB, Tween 80, a hydrophilic surfactant with an HLB of 15 was added to the continuous phase in a Span 80:Tween 80 (v/v) ratio of 84:16, giving an effective HLB of 6. For applications involving delicate biological samples, such as virus emulsification and downstream droplet interaction with cells or antibodies, Tween 80 was removed from the surfactant mix as a precaution to avoid potential adverse interactions between biological components and high concentrations of water-soluble surfactant.[133]

As a result, emulsions produced using the planar flow-focusing droplet generators were stable, exhibiting minimal coalescence and remaining reasonably monodisperse for up to one week after creation. However, coalescence rates increased over time due to sedimentation and Ostwald ripening.[131] To minimize coalescence, emulsions were used within 24 hours of creation.

The emulsions produced using the planar flow-focusing devices had an aqueous volume fraction of 25%. For every 1 μL of emulsion, there were approximately 82,000 droplets of 18 μm diameter. For droplet merging experiments, 300 μL of mineral oil containing 5% surfactant was added to every 20 μL of emulsion, resulting in a final aqueous volume fraction of 1.56%.

Droplet merging in microwell arrays

To perform droplet merging, 13 x 13 microwell array chips, previously used for the digital focus assay described in Chapter 2 were used as the platform. For the initial demonstration experiments, the microwells were fabricated with embedded Pluronic

and filled with DI water, then stored overnight as previously described to enhance hydrophilicity. PBS was then flowed into the device, replacing the DI water and filling the microwells. For demonstration purposes, fluorescent emulsions were created with 10 mM calcein (Millipore Sigma) in PBS as the aqueous phase, and mineral oil containing 5% surfactants as the continuous phase. The emulsion was collected, diluted as described above, loaded into a 1 mL plastic syringe mounted on a syringe pump, and interfaced with the inlet port of the microwell array chip. The emulsion was flowed into the device at a rate of 20 µL/min, which caused complete discretization of the microwell array, with the channel containing the emulsion while the microwell volumes retained PBS. Because the aqueous phase is denser than the continuous oil phase, droplets in the emulsion were allowed to sediment over the discretized microwells for a period of 30 minutes. Fig 3.3 shows image sequence over 30 minutes illustrating the sedimentation of the water droplets onto the discretized microwells.

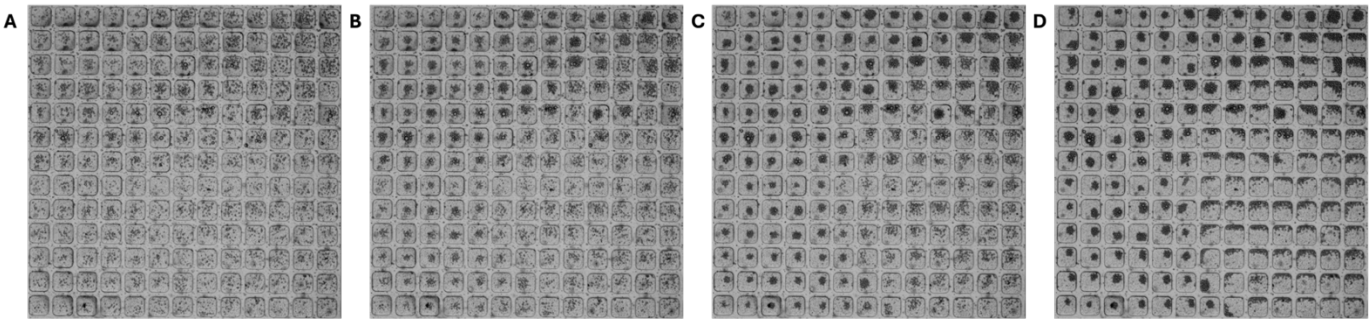


Figure 3.3. Image sequence showing sedimentation of droplets in a water-in-oil emulsion over discretized 200 µm microwells prefilled with water, captured at (A) 0 minutes, (B) 5 minutes, (C) 15 minutes, and (D) 30 minutes after initial discretization.

Due to the concave meniscus interface at the top surface of the discretized microwell, droplets sediment and aggregate near the center of each well. At this stage, a separate

1 mL syringe was filled with surfactant-free mineral oil and interfaced with the inlet port of the discretized microwell chip. Care was taken to ensure that no air bubbles were introduced into the chip during input switching. The surfactant-free oil was infused into the chip at a low, controlled rate of 0.2 μL/min using the syringe pump, minimizing disruption to the sedimented droplets over the microwells. As the surfactant-free oil flowed into the chip, it gradually diluted the surfactant concentration in the emulsion. Over time, the surfactant-free oil mixed with the continuous phase of the emulsion, reducing the effective surfactant concentration. The first droplets at the upstream end of the microwell array began to spontaneously merge with the underlying discretized microwell approximately 30-40 minutes after initiation of surfactant-free oil infusion.

The mechanism for this behavior is related to interfacial energy changes in the system. Hydrophilic surface treatment of PDMS lowers the solid-water interfacial energy, allowing water to wet the microwell walls strongly and produce a low contact angle at the edges. The surfactants in the oil phase lower the oil-water interfacial tension, allowing the pinned interface to adopt greater curvature. Together, these effects cause the oil-water interface to curve downward into the water phase, creating a stable, lower-energy space atop the curved meniscus where droplets in the emulsion preferentially sediment.

For the initial proof-of-concept experiments with fluorescently labeled droplets, the microwell array was imaged under a fluorescence microscope. Delivery of the reagent

to the discretized microwell was confirmed by observing the spreading of fluorescence across the microwell volume as the droplet merged with the well contents. Fig 3.4 shows image sequence over 75 minutes illustrating the merging of the sedimented droplets with the discretized microwells beneath, driven by temporal reduction of surfactant concentration.

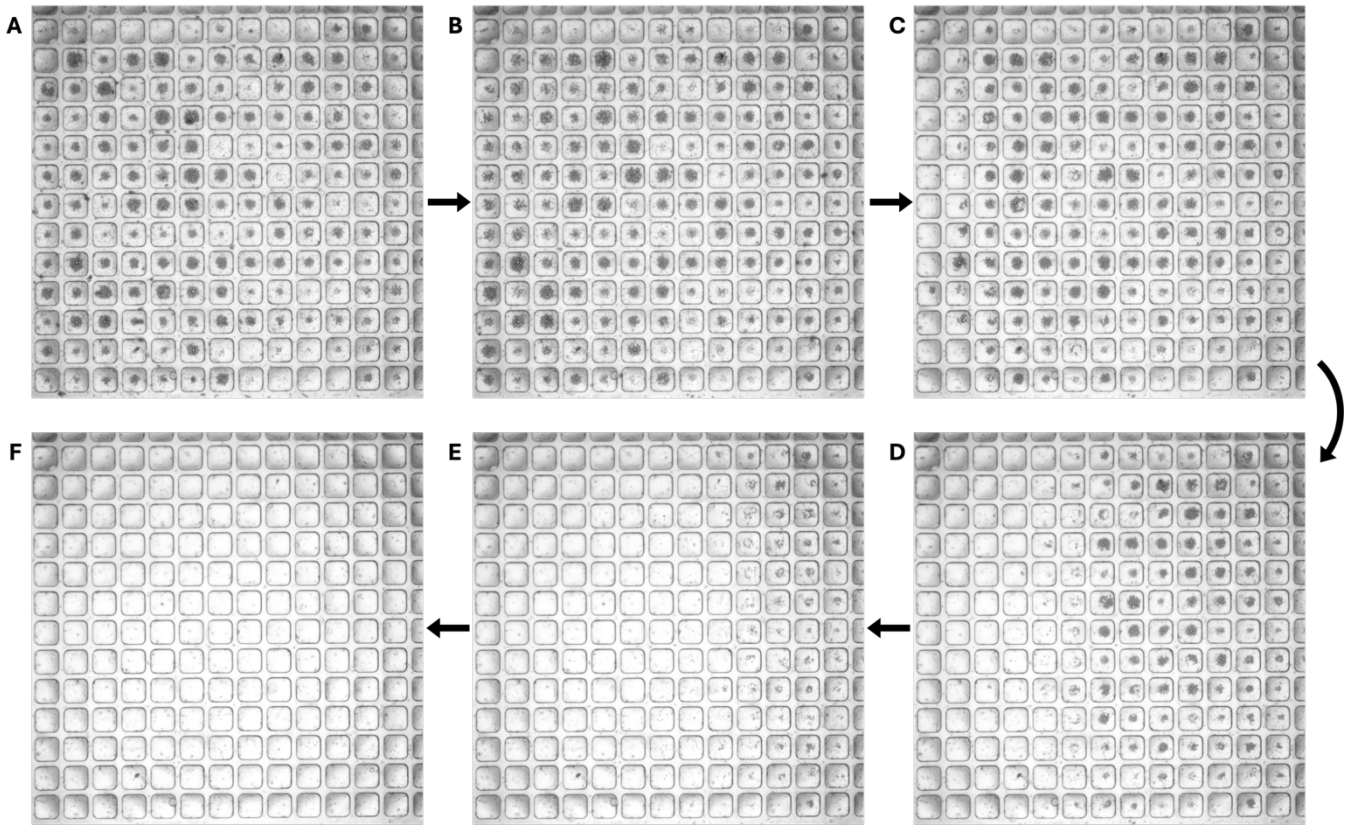


Figure 3.4. Image sequence showing droplet merging of the emulsion with discretized microwells, captured at (A) 0 minutes, (B) 20 minutes, (C) 45 minutes, (D) 55 minutes, (E) 60 minutes, and (F) 75 minutes after the start of surfactant-free oil flow into the chip at 0.2 µL/min. The oil flows from left to right in each image. Due to the pulsatile nature of the oil flow, sedimented droplets are better retained and less susceptible to loss from drag and lift forces.

Demonstration of the droplet merging technology using a bead-based sandwich assay

An assay initially considered for demonstrating the droplet merging technology for single-particle analysis was analogous to a sandwich ELISA, designed to detect and quantify the presence of virus within droplets. The approach involved filling the microwells with magnetic beads functionalized with antibodies to capture the viral antigen delivered via droplet merging. A permanent magnet placed beneath the microfluidic device retained the magnetic beads within the microwells during liquid exchange through the channel. As a result, the beads remained confined in the microwell volume throughout all stages of the process, during initial discretization with the viral emulsion, flushing of the oil phase after droplet merging, and the sequential introduction and washing of the primary and secondary antibodies.

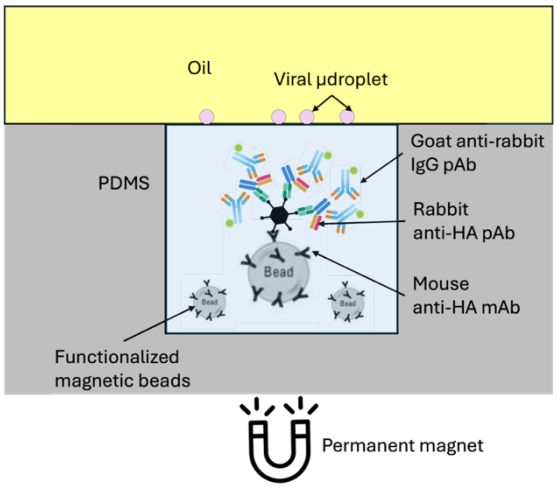


Figure 3.5. Schematic of the functionalized magnetic bead-based sandwich assay. NHS-activated beads are functionalized with a capture antibody (mouse anti-HA monoclonal antibody) and loaded into the microwells, where they are secured in place using an external permanent magnet. PR8 influenza virus is delivered to the microwells through droplet merging. A rabbit anti-HA polyclonal antibody is then flowed into the device, binding to multiple epitopes on the captured PR8 virus particles. Finally, a goat anti-rabbit IgG polyclonal antibody conjugated to a fluorophore is introduced, binding to the immobilized rabbit antibodies and enabling visualization of the captured virus through signal amplification.

Activated magnetic beads containing N-hydroxy-succinimide (NHS) functional groups (Pierce NHS-Activated Magnetic Beads, ThermoFisher) were used as the base substrate for the experiments. These functionalized beads react with primary amines on antibodies to form stable covalent amide linkages. The capture antibody used was a monoclonal antibody specific to the H1N1 PR8 hemagglutinin (Influenza A H1N1 Hemagglutinin / HA Antibody, Mouse Mab, SinoBiological). This antibody was conjugated to the magnetic beads following the manufacturer's protocol, yielding 300 µL of antibody-coupled magnetic beads at a concentration of 10 mg/mL in a storage buffer consisting of 50 mM borate buffer with 0.05% sodium azide. The beads were stored at 4 °C until use.

For detection, a polyclonal rabbit anti-HA antibody (Influenza A H1N1 Hemagglutinin / HA Antibody, Rabbit PAb, SinoBiological) was used as the primary antibody to recognize multiple epitopes on the viral HA antigen. A secondary detection antibody (Goat anti-Rabbit IgG (H+L) Cross-Adsorbed Secondary Antibody, Alexa Fluor™ 488, ThermoFisher), also polyclonal, was then used to bind multiple epitopes on the rabbit IgG molecules. This multilayered approach enhanced signal amplification, as multiple secondary antibodies could bind to each primary antibody, increasing assay sensitivity for low antigen levels. However, the use of polyclonal antibodies reduced specificity due to their broader epitope recognition. Fig 3.5 illustrates the conceptual workflow of the magnetic bead-based assay for viral antigen detection.

A proof-of-concept demonstration of the assay was performed by diluting 10 µL of the stock functionalized magnetic beads in 300 µL of storage buffer in three separate vials. The supernatant was removed using a magnetic stand, and 300 µL of PR8 virus at concentrations of 5E3 FFU/mL, 5E2 FFU/mL, and a negative control containing no virus were added to the respective vials. The mixtures were incubated for 1 hour at room temperature and then overnight at 4 °C, after which the supernatants were discarded. The beads were washed twice with blocking buffer (PBS-T containing 1% BSA) using the magnetic stand. Then, 300 µL of the primary antibody, diluted 1:1000 in blocking buffer, was added to each vial and incubated for 1 hour. Following incubation, the supernatants were discarded and the beads were washed twice with blocking buffer. Next, 300 µL of the secondary detection antibody, diluted 1:500 in blocking buffer, was added to each vial and incubated for 1 hour, followed by discarding the supernatants and washing twice more with blocking buffer. Finally, 5 µL of the magnetic bead suspension was dispensed onto a glass slide and imaged under a fluorescence microscope to compare the relative fluorescence intensity among the three samples.

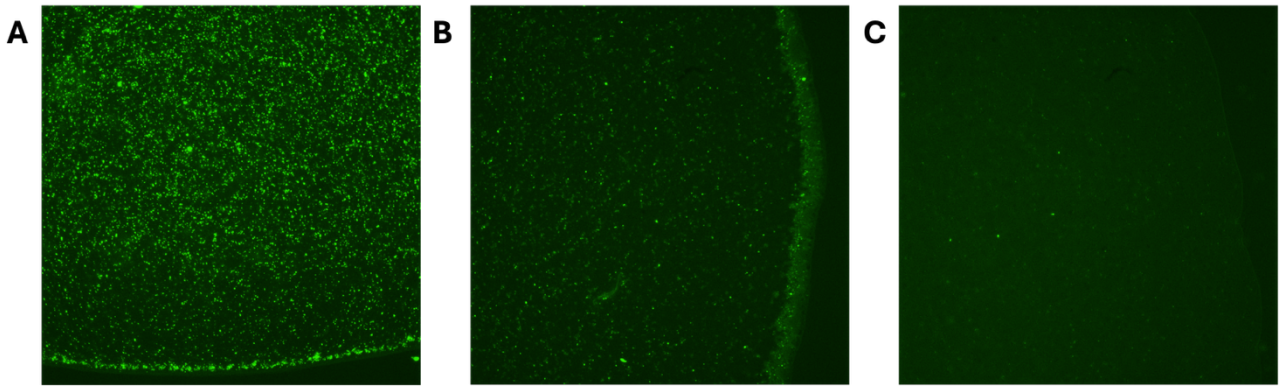


Figure 3.6. Fluorescence intensity of stained functionalized magnetic beads as a function of viral load. Images show fluorescence from beads incubated with (A) 5E3 FFU/mL, (B) 5E2 FFU/mL, and (C) negative control (0 FFU/mL).

The results, as shown in Fig. 3.6 followed the expected trend, with both the fluorescence intensity and the number of fluorescent beads being highest in the first sample containing the highest viral load, followed by the second sample with a 10-fold lower viral load. The control sample exhibited no fluorescence except for a few isolated spots, which were likely due to non-specific binding of antibodies during incubation. These observations suggest that more robust blocking steps may be required. Minimizing background fluorescence from the beads is critical, particularly given the goal of detecting virus at very low concentrations, potentially down to the single-particle level. Therefore, it is essential that any observed fluorescence originates solely from the presence of the viral antigen and not from non-specific antibody binding.

With the proof-of-concept demonstrations yielding promising results, the next step was to assess the feasibility of using the functionalized magnetic beads to determine the distribution of virus in emulsions at the single-particle level. The magnetic bead stock was diluted 1:30 in storage buffer and seeded into the microwells, following a procedure similar to the MDCK cell seeding method described in Chapter 2. A neodymium bar magnet (20 x 10 x 5 mm) was positioned beneath the microfluidic chip, centered on the microwell array, to promote sedimentation of the magnetic beads into the wells.

The PR8 viral stock, at a concentration of 5E4 FFU/mL, was emulsified using the planar flow-focusing droplet generator, producing 18 μm droplets of virus-containing aqueous phase dispersed in mineral oil stabilized with 5% Span 80. Tween 80 was

omitted from the surfactant mixture, as described previously, to avoid potential negative effects of high concentrations of water-soluble surfactant on the virus and other biological materials in the system. The collected emulsion was further diluted with 5% (v/v) surfactant oil at a 20:300 (v/v) ratio.

The diluted viral emulsion was introduced into the microwell chip, where wells containing magnetic beads had been discretized. A negative-control emulsion containing only DMEM medium (no virus) was prepared in parallel. Droplets were allowed to sediment over the microwells for 30 min, after which droplet merging was initiated by flowing surfactant-free mineral oil at 0.2 μL/min. Merging was completed within 60-75 min. Upon completion, the chip was incubated for 1 h at room temperature and then stored overnight at 4 °C. With the chip positioned over a permanent magnet to confine the magnetic beads, the oil overlay was flushed out, and the primary and secondary antibodies were introduced sequentially into the chip, with each incubation lasting 1 h. Blocking buffer was flowed into the device between each step. Finally, the chip was imaged by fluorescence microscopy to detect bead-associated signal within the microwells.

Results

Collection of aerosols as emulsions using CGT

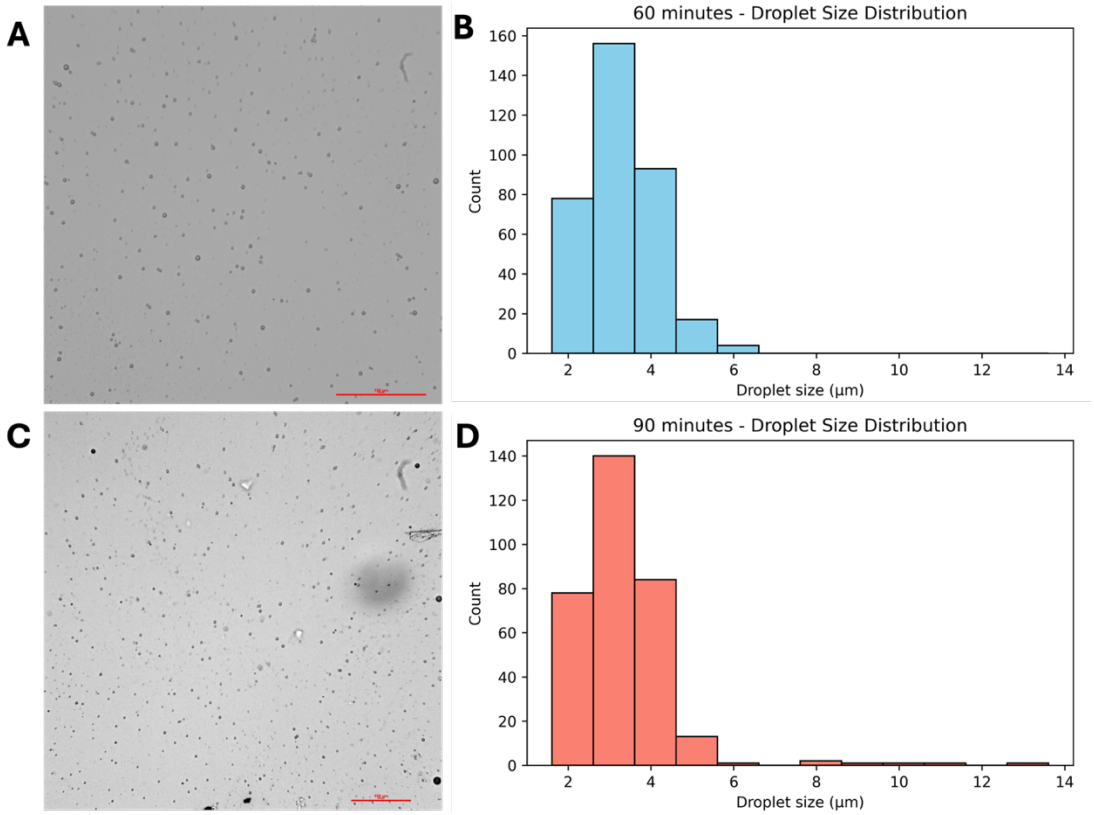


Figure 3.7. (A) Microscopy image showing aerosols collected as droplets in oil using the BioSpot VIVAS condensation growth tube system, sampled over 60 minutes. (B) Corresponding size distribution histogram. (C) Microscopy image showing aerosols collected as droplets in oil using the BioSpot VIVAS condensation growth tube system, sampled over 90 minutes. (D) Corresponding size distribution histogram.

The mean droplet sizes as shown in Fig. 3.7 were similar for the two collection windows (3.28 µm for 60 min and 3.37 µm for 90 min). However, the 60-min emulsion exhibited a smaller standard deviation (0.86 µm) compared with the 90-min emulsion (1.23 µm). This broader spread in the 90-min sample is also evident from outliers up to 13.2 µm, whereas the largest droplet observed in the 60-min sample was 6.4 µm.

Distribution of the sedimented droplets over discretized microwells

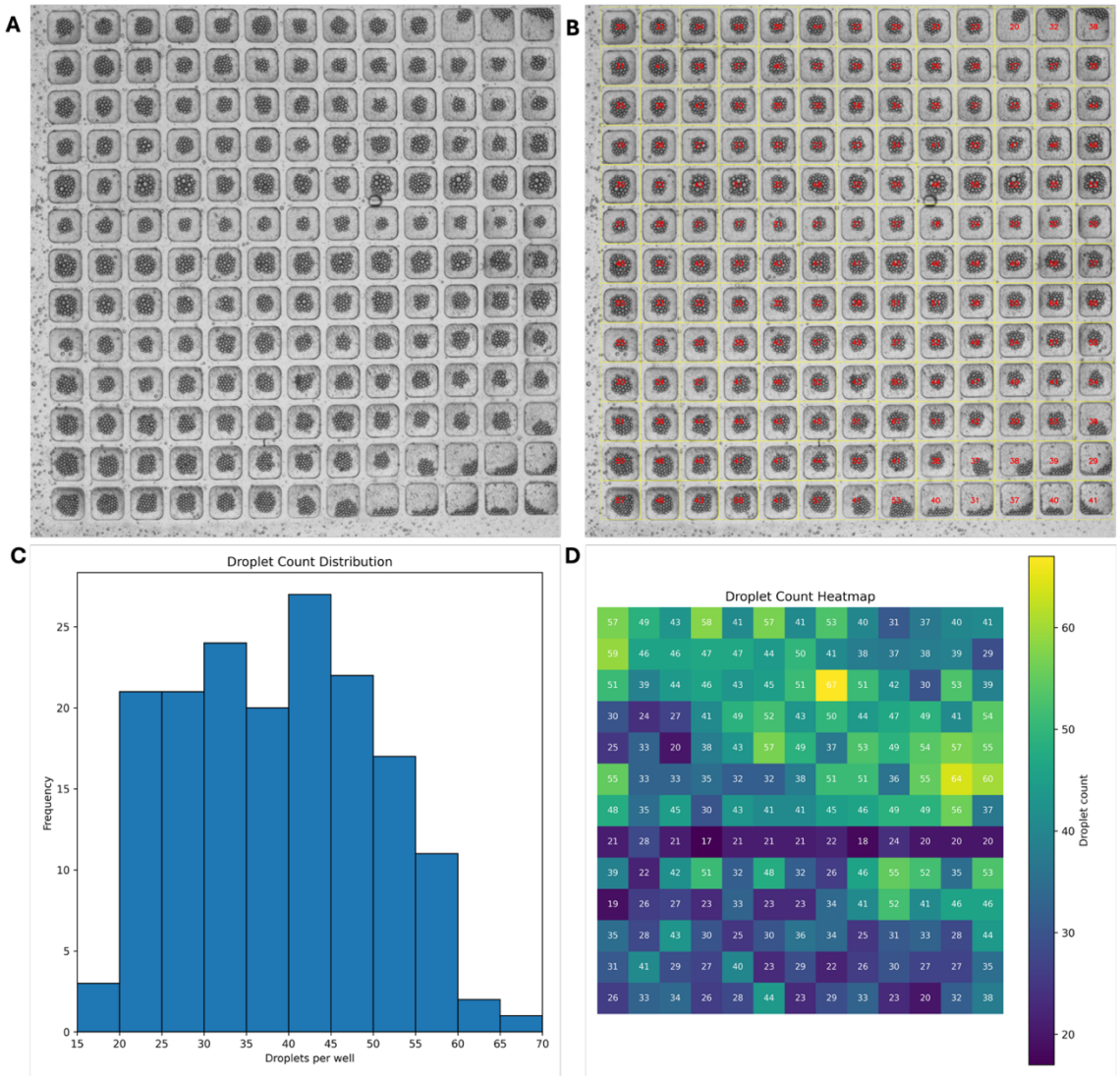


Figure 3.8. (A) Representative image of droplets in emulsion sedimented over a discretized microwell array. (B) Image analysis of (A) showing the number of droplets in each ROI corresponding to a single microwell. (C) Droplet count histogram (bin size = 5) showing the distribution of droplets across the array. (D) The same data visualized as a heatmap, with droplet counts overlaid on individual ROIs.

Fig. 3.8 shows the sedimented droplets across the 169 microwells in the array. The average droplet count was ~38 per microwell (SD = 11), meaning most microwells contained roughly 25-50 droplets. The distribution was symmetric and unimodal,

indicating an even spread without bias toward higher or lower extremes. This moderate variability suggests that the droplet seeding process is stable, with only occasional deviations from the typical count. Consequently, this approach naturally introduces normal variation in the dose delivered to individual microwells, enabling testing across a wider range of input conditions.

Droplet merging

Droplet merging with the discretized microwells occurred as the effective surfactant concentration in the emulsion fell below a critical threshold during the surfactant-free oil infusion. The merging front propagated downstream across the array over ~30-40 min, and the process concluded ~75 min after initiating the surfactant-free oil flow.

To estimate the viral load delivered to each microwell, the following calculations were made. Assuming each well received approximately 38 droplets of 18 μm diameter, corresponding to a total volume of 1.16E-7 mL per well. Given the PR8 stock concentration of 5E4 PFU/mL, the estimated infectious viral load delivered to a single microwell is approximately 5.8E-3 PFU. Literature reports indicate that one FFU can correspond to approximately ten influenza virus particles (FFF-MALS),[134] so the estimated average number of viral particles delivered is ~0.058 particles/well. Using a Poisson model ($\lambda = 0.058$), across 169 wells, only ~9-10 wells would be expected to be contain fluorescence beads on average.

Discussion

Aerosol collection as emulsion

Data from these preliminary experiments demonstrate that aerosols can be successfully collected as emulsions in oil while maintaining the discrete nature of the droplet contents. However, longer sampling times increase the likelihood of droplet coalescence due to increased mixing and agitation during collection, which leads to the formation of larger droplets. This is not ideal for determining the composition of individual droplets, making shorter sampling durations preferable.

Exhaled breath aerosol particles containing respiratory viruses such as influenza are typically contained in droplets that also contain salts, proteins, and surfactants. These additional components can influence droplet stability and behavior. One concern when modeling such droplets with synthetic emulsions is whether the presence of biological material in real aerosols could alter the merging dynamics. In practice, this is likely not a major issue because the original aerosol particles are only tens to hundreds of nanometers in diameter. As they pass through the condensation growth tube (CGT), their volumes increase substantially through water condensation, often reaching several microns in size. This large volume expansion dilutes any natural surfactants or proteins originally present to the point where their effects on droplet stability or merging behavior should be minimal.

A more significant concern arises after growth, when the viruses are effectively suspended in deionized water rather than in their original biological matrix. In the air, the salts, proteins, and surfactants present in exhaled droplets help maintain viral viability. Similarly, traditional collection methods, such as capturing aerosols in virus transport medium (VTM), preserve viability by providing stabilizing components. By contrast, prolonged storage and transport of virus-laden droplets in water-based emulsions could negatively affect viral stability, especially given the hours that may elapse between collection and analysis by droplet merging. To address this limitation, future designs could incorporate collection strategies that better maintain viral integrity. For example, collection in an oil phase with downstream integration into a droplet-merging platform would allow immediate analysis after sampling while minimizing losses in viral viability during handling and storage.

Another technology with strong potential for single-aerosol analysis is digital qRT-PCR combined with droplet discretization. By merging collected aerosol droplets in oil with droplets containing PCR reagents, individual amplification reactions could be performed, enabling quantification of viral RNA at the single-droplet level and providing detailed insight into the distribution of viral genomes across aerosol particles. This dissertation did not pursue digital PCR because the primary aim was to develop a platform capable of addressing not only the distribution of viral RNA but also the distribution of *viable* viruses. Understanding viability requires integration with cell culture systems, where the contents of individual droplets can be delivered to host cells for infectivity testing. The magnetic bead-based sandwich assay served as an

intermediate demonstration of the droplet merging platform, with the long-term goal of coupling this approach to digital focus assays (dFA) for viability analysis. Nevertheless, digital PCR remains a powerful and complementary strategy. While it does not capture viability, it offers high sensitivity for RNA detection and could be directly applied to condensation growth tube (CGT)-based aerosol collections to map viral genome distribution at the single-particle level.

Droplet merging issues

One issue observed during the initial droplet merging experiments was the unintended loss of sedimented droplets to the flow of surfactant-free oil. At higher flow rates, more droplets were carried away due to the drag force exerted by the oil flowing in the channel above the microwells. A flow rate of 0.2 µL/min was ultimately selected after multiple trials with varying flow rates, as it provided the best balance between minimizing droplet loss and maintaining a reasonable merging time.

An additional observation was made during experiments performed with a different syringe pump (Fusion 400, Chemyx), where the surfactant-free oil exhibited a periodic, pulsatile flow behavior. This was attributed to operating the pump at the lower end of its flow rate range. For a 1 mL syringe at 0.2 µL/min, the pump's stepper motor, which drives the pusher block via microstepping, operates at its step resolution of 0.016 µm/µstep.[135] This corresponds to a minimal linear displacement of the plunger that delivers approximately 0.03 µL of liquid per microstep. To sustain a flow rate of 0.2

μL/min, the pump actuates once every 8.6 seconds, resulting in the pulsatile flow pattern observed under the microscope. Because the volume delivered per step is small and does not generate sufficient force to dislodge the sedimented droplets from the concave microwell meniscus, the droplets remained stably positioned, with minimal loss during the surfactant-free oil flow.

Issues with the sandwich assay

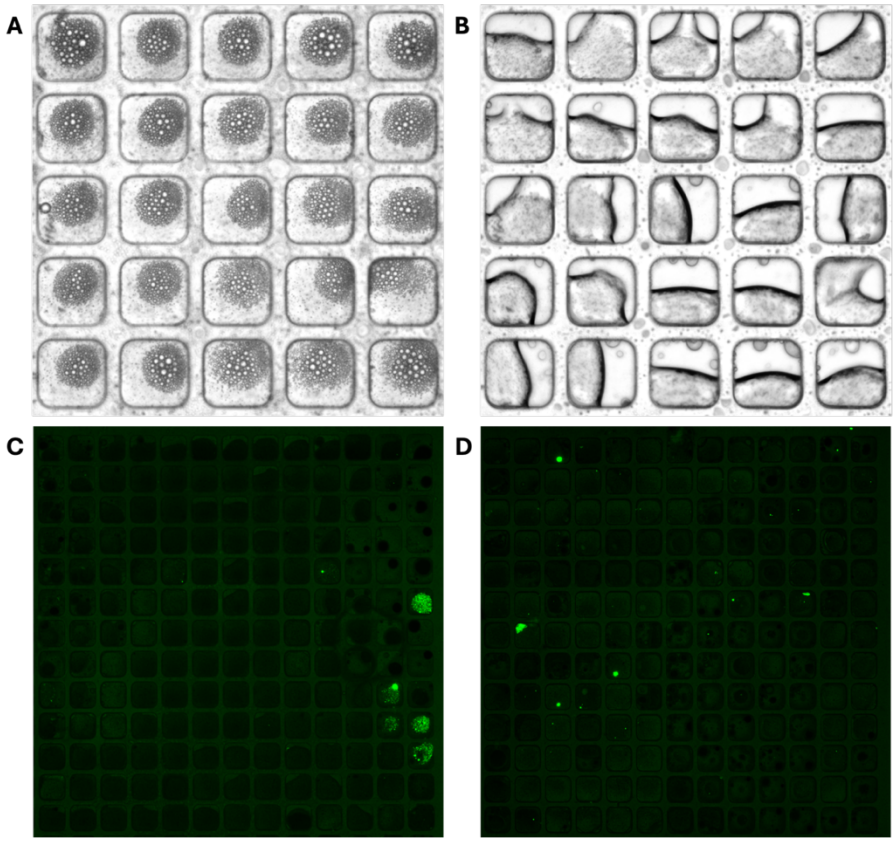


Figure 3.9. (A) Sedimented PR8 virus-containing droplets over discretized microwells loaded with functionalized magnetic beads. (B) Microwell array after completion of droplet merging, showing dewetting but no loss of magnetic beads. (C) Fluorescence microscopy image of the microwell array after antibody staining post-droplet merging, where the delivered droplets contained virus at 5E4 FFU/mL. (D) Fluorescence microscopy image of the microwell array after antibody staining for a negative control device post-droplet merging, where the delivered droplets contained no virus.

The calculations for estimating the number of positive wells through Poisson statistics using the bead-based sandwich assay are based on several compounded assumptions, including droplet size, the number of droplets merging into a given well, and the effective viral dose delivered. The resulting estimate should therefore be interpreted cautiously and viewed primarily as an exercise to approximate the expected number of positive wells rather than as a definitive measurement. A central assumption concerns the conversion between traditional quantification units and particle numbers. Literature has reported that one focus-forming unit (FFU) can correspond to approximately ten influenza virus particles. However, this relationship is itself based on multiple assumptions and is unlikely to hold consistently across different influenza strains. Factors such as the method of virus collection, propagation conditions, the number of freeze-thaw cycles, and the host cells used for titration can all influence the apparent ratio between infectious units and physical particles. While the cited 1:10 ratio is often applied to influenza virus, the true ratio can vary substantially and is frequently much higher for other viral infections. Thus, while this estimation provides a useful framework for contextualizing the number of positive wells after droplet merging, it is important to recognize its limitations. Careful consideration is needed when extending such calculations to different influenza strains or other viral pathogens, where particle-to-infectious unit ratios may differ significantly.

Several issues were encountered during the droplet merging experiments as shown in Fig. 3.9. Most notably, the presence of magnetic beads inside the microwells led to unexpected water loss from the microwell volume, even though the beads themselves

remained confined. This effect was not observed in identical devices used for the proof-of-concept demonstrations or the MDCK cell seeding experiments, where the aqueous phase remained stable. In the present experiments, however, the aqueous phase in some microwells began to partial dewet one or more microwell edges, resulting in a gradual decrease in water volume during the merging process as shown in Fig. 3.9 (B).

The exact cause of this phenomenon remains unclear, but it may be linked to the surface chemistry of the functionalized magnetic beads interacting with both the emulsions and the surfactant-laden oil phase. Despite the partial loss of aqueous volume, the beads remained stably confined, allowing the staining protocol to be completed.

In an effort to address background fluorescence, the concentration of Tween 20 in the blocking buffer was increased from 0.05% to 0.1%, and BSA from 1% to 3%. However, the problem persisted. Background fluorescence was observed in approximately half of the microwells in the negative control emulsion as shown in Fig 3.9 (D). While PR8 samples produced 4 to 10 brightly fluorescent microwells as shown in Fig 3.9 (C), more robust and reproducible data, along with improved blocking strategies will be required before making definitive conclusions regarding the sensitivity or quantitative capabilities of this platform for influenza virus detection.

Acknowledgements

I gratefully acknowledge Arantzazu Eiguren-Fernandez and Gregory S. Lewis (Aerosol Dynamics Inc.) for their input on aerosol sampling technology, and Sheldon Tai,

Margaret A. Scull, and Don L. DeVoe for their valuable guidance, support, and resources during the development of this work.

Chapter 4: Conclusion and Future Directions

Conclusions

The primary objective of this dissertation was to develop and demonstrate microfluidic technologies that improve the speed, cost-effectiveness, and ease of use for viral quantification and characterization, with an emphasis on viable virus quantification and the analysis of aerosols for single-particle resolution. Two complementary platforms were created toward this goal: a digital focus assay (dFA) for accurate and cost-effective quantification of infectious virus, and a droplet merging platform to enable compositional analysis of bioaerosols.

The dFA platform successfully combined nanoliter-scale cell culture arrays, oil overlay-based isolation, and automated image analysis to deliver accurate viral titers using substantially reduced sample and reagent volumes compared to conventional assays. This approach provides a foundation for improved assay automation, flexible endpoint timing, and broad applicability across both laboratory and clinical samples, as demonstrated with model and clinical influenza A viruses.

The droplet merging platform works toward answering fundamental questions in aerovirology by establishing methods to collect aerosols as discrete droplets in oil and merge them in a controlled manner with assay reagents. Proof-of-concept studies demonstrated the feasibility of merging single or small groups of droplets for

downstream analysis, laying the groundwork for future single-particle-level investigations into viral distribution within aerosols and the quanta of infection.

Together, these platforms expand the resources available for infectious disease research, bridging gaps between conventional bulk assays and digital microfluidic approaches. Their potential impact spans clinical diagnostics, vaccine development, environmental surveillance, and fundamental aerovirology, offering cost-effective, versatile, and convenient solutions for quantifying and characterizing viruses in both research and real-world settings.

Future directions

Improvements to the dFA platform

Opportunities remain for further optimization of the dFA platform. For our current chip design with 169 wells, the confidence interval range increases dramatically as the positive well fraction approaches the lower ($\hat{p} \rightarrow 0$) and upper ($\hat{p} \rightarrow 1$) limits and the confidence interval limits remain within ±50% of the mean concentration value when $0.10 < \hat{p} < 0.96$. Depending on the required assay range and precision, it may be desirable to increase the number of microwells in the array in order to reduce measurement uncertainty and extend the limits of detection. For the current microwell array design, the theoretical range of detection that maintains a ±50% confidence interval corresponding to a range of positive well fractions given by $0.10 < \hat{p} < 0.96$ is between 1.1×10^4 and 3.4×10^5 PFU/mL. In contrast, by combining data from 3 chips yielding a total of 507 wells, the same confidence interval limits are achieved for $0.03 < \hat{p} < 0.99$. In this case, the detection range is extended to between 3.2×10^3 and

4.8 x 10^5 PFU/mL. Enhanced detection limits can also be achieved by increasing the well volume through modifications to the microwell geometry. Increasing the depth of the microwells allows for greater pathogen sampling per well and provides a larger volume of medium to support cell culture, enabling longer incubation times for assays that require it. To create devices with greater array density and higher well counts, the design must be further optimized before expanding the array area, as seeding heterogeneity tends to increase near the channel edges. Incorporating passive elements, such as improved pillar array designs and other structural features, will be important for improving seeding uniformity.

Other improvements can enhance end-user comfort and convenience, including enabling a flexible assay endpoint time. In traditional cell culture based viral quantification assays with fixed endpoints, the experiment must be stopped at a predetermined time, typically by washing away the overlay and fixing the cells, to limit the number of viral replication cycles. Missing this time point can lead to unreliable results. Because the dFA has a digital readout and each microwell is isolated, it can, in principle, support a flexible endpoint, allowing the experiment to be stopped within a broader time window without compromising accuracy. Validating the dFA for multiple endpoint times beyond the current 24-hour standard would expand its utility.

Another modification to improve usability is replacing syringe pump or pneumatic driven flow with traditional wet lab tools, such as pipettes, to make operation easier and faster for untrained users. The main challenge with this change is preventing air

bubbles from entering the channel, as these can disrupt the experiment, sometimes irreversibly. While adapting the inlet to accept pipette tips is straightforward, the device should also be designed to make bubble removal simple or to prevent bubbles from affecting the microwells. This could involve design changes such as extending or making the roof of the microwell channel convex, preventing buoyant air bubbles from becoming trapped. Such features could be implemented through simple multilayer SU-8 patterning, as described in Chapter 2.

A further necessary modification is ensuring the chip does not dry out during incubation at 37 °C and 5% CO_2, as drying has been observed to cause assay failure in past experiments. One option is to seal the inlet and outlet channels to prevent evaporation of oil or medium. Alternatively, as demonstrated in a working prototype as shown in Fig. 4.1, a third PDMS layer can be bonded over the chip with large holes punched around the original inlet and outlet ports to act as liquid reservoirs, preventing chip dry-out.

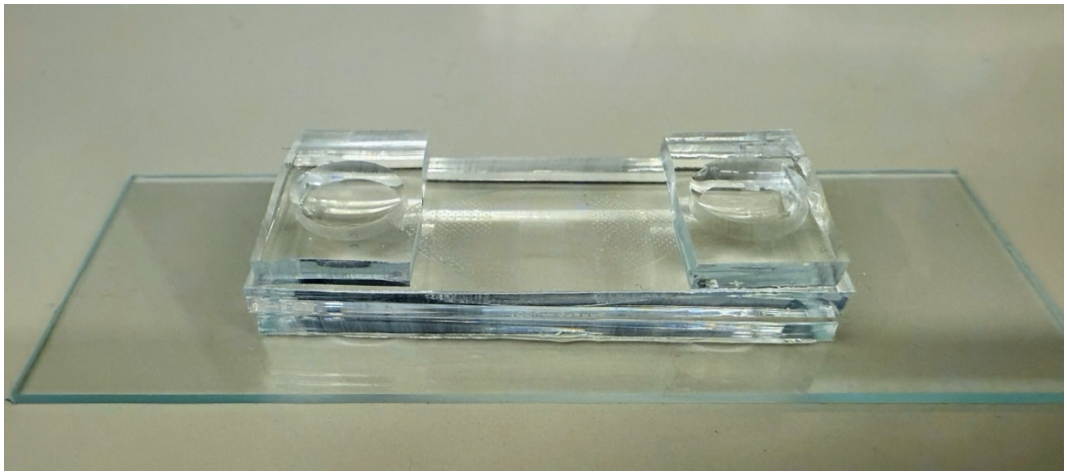


Figure 4.1. Image of the prototype dFA chip with reservoirs over the inlet and outlet ports to hold excess media and oil, preventing chip dry-out.

A safety-related modification to the integrated format of the microfluidic device can also benefit the characterization of higher biosafety level pathogens, where eliminating sharps is desirable to reduce operator risk. For example, sharps can be removed from the design by replacing the glass substrate, used as a rigid chip support, with a thermoplastic layer. Likewise, the blunt needle interface used for fluid delivery through the chip can be replaced with an elastomeric pipette interface to support manual or automated delivery of media, samples, and reagents. In addition, the compact chip format can allow assays to be operated within an enclosed chamber or holder to reduce the risk of bioaerosol formation.

Improvements to the Droplet Merging Platform

Further optimization of the droplet merging platform requires systematic evaluation of aerosol collection as emulsions in CGT systems under varied sampling conditions. Parameters such as ambient humidity, temperature, aerosol concentration, and collection duration are likely to influence both the size distribution and stability of collected droplets. While theoretical considerations indicate that higher initiator temperatures and steeper temperature gradients in the CGT column produce larger droplets, direct experimental validation is necessary to quantify how the temperature of each CGT section influences droplet size. It is also essential to characterize viral stability in collected emulsions over different storage durations to define the maximum permissible delay between sample acquisition and downstream analysis.

In addition to mineral oil, fluorinated oils such as FC40 and HFE7500 warrant investigation due to their excellent biocompatibility and demonstrated ability to form

stable emulsions with fluorosurfactants, a formulation widely employed in droplet PCR. The primary drawbacks of these oils are their higher cost and density, which causes aqueous droplets to float at the oil surface. This accumulation can lead to droplet coalescence during inertial impaction collection, potentially compromising sample integrity. To address this, the collection container design should be modified to ensure that newly collected droplets do not land directly on previously deposited ones, maintaining discrete encapsulation.

Finally, to improve droplet generation throughput, particularly for assays involving live virus, alternative emulsion generation platforms should be considered. Current planar flow-focusing devices may require 1-2 days to produce sufficient volume, risking loss of viral infectivity. High-throughput droplet generation methods capable of producing monodisperse emulsions at rates >100 kHz,[136] could significantly reduce processing time and preserve sample viability.

Improvements to Magnetic Bead-Based Assay

To improve the utility of the magnetic bead-based assay, strategies that reduce non-specific background fluorescence must be systematically pursued. Approaches include optimizing blocking buffer formulations, by adjusting concentrations of Tween-20, BSA, or incorporating heat-inactivated serum, and FBS, known to minimize background in immunofluorescence. Rigorous titration of each component is essential to balance reduced background with preserved target binding. Another approach is to replace polyclonal antibodies (pAbs), which bind multiple epitopes and may elevate background, with monoclonal antibodies (mAbs) that offer high specificity and

reproducibility, albeit at potentially lower overall sensitivity. A complementary strategy is dual-marker detection, such as staining for an additional viral protein like neuraminidase (NA) in a separate spectral channel and confirming the signal through co-localization. True viral signals should co-localize, whereas non-specific background typically does not, thus enhancing confidence in assay specificity.

Combining the dFA platform with droplet merging

Finally, beyond detecting viral proteins using the magnetic bead-based assay, this platform could be adapted to assess the distribution of viable viruses within aerosol-derived droplets. In this approach, the microwells would be seeded with cultured cells, similar to the dFA platform, but instead of delivering virus in a homogeneous bulk medium, virus-containing droplets would be merged directly into the wells. The ensuing infections could be identified via nucleoprotein (NP) immunostaining, and spatial mapping of positive wells would reveal the distribution pattern of infectious particles within the aerosol sample.

For this application, an array of smaller, densely packed microwells would offer clear advantages over the current 200 μm design, which contains only 169 wells. Because the volume of individual droplets is several orders of magnitude smaller than the volume of the 200 μm wells, droplet delivery into such large wells leads to substantial dilution of viral particles, potentially limiting the accuracy of quantification. A denser microwell array would not only reduce dilution effects but also increase the total

number of independent measurements, thereby improving statistical power for characterizing viral distribution.

The improvements outlined in this chapter provide a roadmap for enhancing the sensitivity, usability, and versatility of the dFA and droplet merging platforms. By incorporating higher-density microwell arrays, adaptable fluid handling, advanced aerosol capture and droplet generation methods, and refined immunoassay strategies, the system can be tailored to a broad range of applications. These include rapid, cost-effective, and user-friendly infectious disease diagnostics, addressing key unanswered questions in aerovirology such as the quanta of infection and viral distribution within aerosols, and enabling quantitative aerosol surveillance across research and clinical settings.

Concluding Remarks and Perspectives

This dissertation leveraged microfluidic discretization for two complementary goals: first, to develop an assay to quantify viable influenza viruses, and second, to create technology for capturing and interrogating viruses at single-particle resolution in order to answer fundamental questions in aerovirology, particularly regarding how viruses are distributed within aerosols. The first part demonstrated how the digital focus assay (dFA) enabled digital quantification of viable influenza virus by discretizing samples into microwells and detecting infection events through immunostaining. The second part introduced how condensation growth tubes can be used to collect single-aerosol

particles as discrete droplets, providing a direct route for interrogating the composition of virus-laden droplets. The latter portion of this work also showcased the droplet merging platform as a flexible tool to fuse collected droplets with detection reagents or cultured cells, providing pathwork for downstream assays of viral content and viability. Together, these tools represent a modular framework for discrete biological particle analysis.

Beyond influenza and aerovirology, the broader implications of these technologies lie in their ability to shift biological measurements from bulk averages to single-particle resolution. By resolving the heterogeneity of individual droplets, these approaches provide mechanistic insights into how incomplete viral genomes complement one another, how co-infection thresholds determine transmission, and how aerosolized particles differ in infectious potential. The same principles can extend to other respiratory pathogens such as RSV, coronaviruses, or other viral and bacterial aerosols, where understanding single-particle infectivity and viability remains an open challenge. More generally, integrating droplet discretization with functional assays establishes a versatile platform applicable to the broader field of microfluidic discretization, particularly for introducing reactants and reagents into discretized micro- and nanowell volumes to carry out diverse reactions and assays.

The scientific contributions of this work are therefore twofold. First, they demonstrate the feasibility of adapting classical virology assays, such as focus-forming assays, into miniaturized digital formats capable of performing measurements at significantly

reduced cost and with added convenience for the end user, through automation and potential for further automation. Second, they show that technologies originally developed for aerosol science, such as condensation growth tube-based sampling, can be used to collect aerosols as single particles and, when coupled with the droplet merging platform, can produce new modes of biological analysis. Together, these advances move the field from descriptive characterization of aerosols toward mechanistic understanding of how infectious agents are packaged, transmitted, and propagated.

Looking forward, several avenues exist to extend and refine this technology. Automated image acquisition and machine learning-based image processing could streamline the digital assays into a fully automated workflow. Redesigned devices that replace syringe-pump-driven flows with simple pipettable interfaces would facilitate adoption by non-specialist laboratories. The droplet merging platform could be integrated with magnetic bead-based immunoassays to study the distribution of viral antigens, or with dFA-based cell culture assays to assess the distribution of viable virus at the single-particle level. Alternatively, collected aerosol droplets could be merged with reagents to perform digital PCR on discrete droplets, enabling analysis of genome distribution across particles. Finally, in the context of pandemic preparedness, these technologies could form the basis of rapid, high-resolution platforms for monitoring airborne transmission of emerging pathogens.

In summary, the body of work presented in this dissertation establishes a set of enabling technologies for the discrete analysis of infectious particles. While motivated by fundamental questions in aerovirology, the broader impacts of these approaches extend across virology, microbiology, biotechnology, and microfluidic engineering. By advancing biological assays toward single-particle resolution, this work opens new opportunities for mechanistic insight, methodological innovation, and practical application in both research and public health.

Bibliography

1. Types of Influenza Viruses | Influenza (Flu) | CDC. Retrieved 15 August 2025 from https://www.cdc.gov/flu/about/viruses-types.html.
2. Influenza (seasonal). Retrieved 15 August 2025 from https://www.who.int/news-room/fact-sheets/detail/influenza-(seasonal).
3. About Estimated Flu Burden | Flu Burden | CDC. Retrieved 15 August 2025 from https://www.cdc.gov/flu-burden/php/about/index.html.
4. Preliminary Estimated Flu Disease Burden 2024-2025 Flu Season | Flu Burden | CDC. Retrieved 15 August 2025 from https://www.cdc.gov/flu-burden/php/data-vis/2024-2025.html.
5. The burden of Influenza. Retrieved 15 August 2025 from https://www.who.int/news-room/feature-stories/detail/the-burden-of-influenza.
6. Smith, A. M. & Perelson, A. S. Influenza A virus infection kinetics: quantitative data and models. *Wiley Interdiscip Rev Syst Biol Med* **3**, 429–445 (2011).
7. Miao, H. *et al.* Quantifying the Early Immune Response and Adaptive Immune Response Kinetics in Mice Infected with Influenza A Virus. *J Virol* **84**, 6687–6698 (2010).
8. Canini, L. & Carrat, F. Population Modeling of Influenza A/H1N1 Virus Kinetics and Symptom Dynamics. *J Virol* **85**, 2764–2770 (2011).
9. Saenz, R. A. *et al.* Dynamics of Influenza Virus Infection and Pathology. *J Virol* **84**, 3974–3983 (2010).
10. Pawelek, K. A. *et al.* Modeling Within-Host Dynamics of Influenza Virus Infection Including Immune Responses. *PLoS Comput Biol* **8**, e1002588 (2012).
11. Hadjichrysanthou, C. *et al.* Understanding the within-host dynamics of influenza A virus: from theory to clinical implications. *J R Soc Interface* **13**, (2016).
12. Baccam, P., Beauchemin, C., Macken, C. A., Hayden, F. G. & Perelson, A. S. Kinetics of Influenza A Virus Infection in Humans. *J Virol* **80**, 7590–7599 (2006).
13. Sidorenko, Y. & Reichl, U. Structured model of influenza virus replication in MDCK cells. *Biotechnol Bioeng* **88**, 1–14 (2004).
14. König, R. *et al.* Human host factors required for influenza virus replication. *Nature 2010 463:7282* **463**, 813–817 (2009).
15. Karlas, A. *et al.* Genome-wide RNAi screen identifies human host factors crucial for influenza virus replication. *Nature 2010 463:7282* **463**, 818–822 (2010).
16. Tellier, R. Aerosol transmission of influenza A virus: a review of new studies. *J R Soc Interface* **6**, (2009).
17. Yan, J. *et al.* Infectious virus in exhaled breath of symptomatic seasonal influenza cases from a college community. *Proc Natl Acad Sci U S A* **115**, 1081–1086 (2018).
18. Cowling, B. J. *et al.* Aerosol transmission is an important mode of influenza A virus spread. *Nature Communications 2013 4:1* **4**, 1–6 (2013).
19. Fabian, P. *et al.* Influenza Virus in Human Exhaled Breath: An Observational Study. *PLoS One* **3**, e2691 (2008).
20. Nikitin, N., Petrova, E., Trifonova, E. & Karpova, O. Influenza virus aerosols in the air and their infectiousness. *Adv Virol* **2014**, (2014).

21. Smith, A. M. *et al.* Effect of 1918 PB1-F2 Expression on Influenza A Virus Infection Kinetics. *PLoS Comput Biol* **7**, e1001081 (2011).
22. Yan, A. W. C. *et al.* Quantifying mechanistic traits of influenza viral dynamics using in vitro data. *Epidemics* **33**, 100406 (2020).
23. Beauchemin, C. A. A. *et al.* Modeling amantadine treatment of influenza A virus in vitro. *J Theor Biol* **254**, 439–451 (2008).
24. Handel, A., Longini, I. M. & Antia, R. Neuraminidase Inhibitor Resistance in Influenza: Assessing the Danger of Its Generation and Spread. *PLoS Comput Biol* **3**, e240 (2007).
25. Matrosovich, M., Matrosovich, T., Carr, J., Roberts, N. A. & Klenk, H.-D. Overexpression of the α-2,6-Sialyltransferase in MDCK Cells Increases Influenza Virus Sensitivity to Neuraminidase Inhibitors. *J Virol* **77**, 8418–8425 (2003).
26. Moss, R. B. *et al.* A Phase II Study of DAS181, a Novel Host Directed Antiviral for the Treatment of Influenza Infection. *J Infect Dis* **206**, 1844–1851 (2012).
27. Furuta, Y. *et al.* In vitro and in vivo activities of anti-influenza virus compound T-705. *Antimicrob Agents Chemother* **46**, 977–981 (2002).
28. Hayden, F. G., Cote, K. M. & Douglas, R. G. Plaque inhibition assay for drug susceptibility testing of influenza viruses. *Antimicrob Agents Chemother* **17**, 865–870 (1980).
29. Mifsud, E. J., Hayden, F. G. & Hurt, A. C. Antivirals targeting the polymerase complex of influenza viruses. *Antiviral Res* **169**, 104545 (2019).
30. Dunn, C. J. & Gon, K. L. Zanamivir: A review of its use in influenza. *Drugs* **58**, 761–784 (1999).
31. Lee, N. *et al.* Viral Loads and Duration of Viral Shedding in Adult Patients Hospitalized with Influenza. *J Infect Dis* **200**, 492–500 (2009).
32. Herrera-Rodriguez, J. *et al.* A novel peptide-based vaccine candidate with protective efficacy against influenza A in a mouse model. *Virology* **515**, 21–28 (2018).
33. Hatta, Y. *et al.* Novel influenza vaccine M2SR protects against drifted H1N1 and H3N2 influenza virus challenge in ferrets with pre-existing immunity. *Vaccine* **36**, 5097–5103 (2018).
34. Eichelberger, M. C., Morens, D. M. & Taubenberger, J. K. Neuraminidase as an influenza vaccine antigen: a low hanging fruit, ready for picking to improve vaccine effectiveness. *Curr Opin Immunol* **53**, 38–44 (2018).
35. Wacheck, V. *et al.* A novel type of influenza vaccine: safety and immunogenicity of replication-deficient influenza virus created by deletion of the interferon antagonist NS1. *J Infect Dis* **201**, 354–362 (2010).
36. Liu, J., Shi, X., Schwartz, R. & Kemble, G. Use of MDCK cells for production of live attenuated influenza vaccine. *Vaccine* **27**, 6460–6463 (2009).
37. Le Ru, A. *et al.* Scalable production of influenza virus in HEK-293 cells for efficient vaccine manufacturing. *Vaccine* **28**, 3661–3671 (2010).
38. Genzel, Y., Dietzsch, C., Rapp, E., Schwarzer, J. & Reichl, U. MDCK and Vero cells for influenza virus vaccine production: A one-to-one comparison up to lab-scale bioreactor cultivation. *Appl Microbiol Biotechnol* **88**, 461–475 (2010).

39. Pau, M. G. *et al.* The human cell line PER.C6 provides a new manufacturing system for the production of influenza vaccines. *Vaccine* **19**, 2716–2721 (2001).
40. Mendelman, P. M., Cordova, J. & Cho, I. Safety, efficacy and effectiveness of the influenza virus vaccine, trivalent, types A and B, live, cold-adapted (CAIV-T) in healthy children and healthy adults. *Vaccine* **19**, 2221–2226 (2001).
41. Karron, R. A. *et al.* Evaluation of two live attenuated cold-adapted H5N1 influenza virus vaccines in healthy adults. *Vaccine* **27**, 4953–4960 (2009).
42. Hawksworth, A. *et al.* Replication of live attenuated influenza vaccine viruses in human nasal epithelial cells is associated with H1N1 vaccine effectiveness. *Vaccine* **38**, 4209–4218 (2020).
43. Debbink, K. *et al.* Vaccination has minimal impact on the intrahost diversity of H3N2 influenza viruses. *PLoS Pathog* **13**, e1006194 (2017).
44. François, A. *et al.* Accurate Titration of Infectious AAV Particles Requires Measurement of Biologically Active Vector Genomes and Suitable Controls. *Mol Ther Methods Clin Dev* **10**, 223–236 (2018).
45. Shiau, A.-L., Liu, P.-S. & Wu, C.-L. Novel Strategy for Generation and Titration of Recombinant Adeno-Associated Virus Vectors. *J Virol* **79**, 193–201 (2005).
46. Mittereder, N., March, K. L. & Trapnell, B. C. Evaluation of the concentration and bioactivity of adenovirus vectors for gene therapy. *J Virol* **70**, 7498–7509 (1996).
47. Lee, N. *et al.* Viral Loads and Duration of Viral Shedding in Adult Patients Hospitalized with Influenza. *J Infect Dis* **200**, 492–500 (2009).
48. Lau, L. L. H. *et al.* Viral Shedding and Clinical Illness in Naturally Acquired Influenza Virus Infections. *J Infect Dis* **201**, 1509–1516 (2010).
49. Hijano, D. R. *et al.* Clinical correlation of influenza and respiratory syncytial virus load measured by digital PCR. *PLoS One* **14**, e0220908 (2019).
50. García-Arroyo, L. *et al.* Benefits and drawbacks of molecular techniques for diagnosis of viral respiratory infections. Experience with two multiplex PCR assays. *J Med Virol* **88**, 45–50 (2016).
51. Wei, Z. *et al.* Biophysical characterization of influenza virus subpopulations using field flow fractionation and multiangle light scattering: Correlation of particle counts, size distribution and infectivity. *J Virol Methods* **144**, 122–132 (2007).
52. Van Elden, L. J. R., Nijhuis, M., Schipper, P., Schuurman, R. & Van Loon, A. M. Simultaneous detection of influenza viruses A and B using real-time quantitative PCR. *J Clin Microbiol* **39**, 196–200 (2001).
53. Schweiger, B., Zadow, I., Heckler, R., Timm, H. & Pauli, G. Application of a fluorogenic PCR assay for typing and subtyping of influenza viruses in respiratory samples. *J Clin Microbiol* **38**, 1552–1558 (2000).
54. Pan, M., Lednicky, J. A. & Wu, C. Y. Collection, particle sizing and detection of airborne viruses. *J Appl Microbiol* **127**, 1596–1611 (2019).
55. Puhach, O., Meyer, B. & Eckerle, I. SARS-CoV-2 viral load and shedding kinetics. *Nature Reviews Microbiology 2022 21:3* **21**, 147–161 (2022).
56. Leirs, K. *et al.* Bioassay Development for Ultrasensitive Detection of Influenza A Nucleoprotein Using Digital ELISA. *Anal Chem* **88**, 8450–8458 (2016).

57. Song, D. S. *et al.* Evaluation of a competitive ELISA for antibody detection against avian influenza virus. *J Vet Sci* **10**, 323–329 (2009).
58. Zhou, E. M., Chan, M., Heckert, R. A., Riva, J. & Cantin, M. F. Evaluation of a competitive ELISA for detection of antibodies against avian influenza virus nucleoprotein. *Avian Dis* **42**, 517–522 (1998).
59. de Boer, G. F., Back, W. & Osterhaus, A. D. M. E. An ELISA for detection of antibodies against influenza A nucleoprotein in humans and various animal species. *Arch Virol* **115**, 47–61 (1990).
60. Meijer, A. *et al.* Measurement of antibodies to avian influenza virus A(H7N7) in humans by hemagglutination inhibition test. *J Virol Methods* **132**, 113–120 (2006).
61. Ohmit, S. E., Petrie, J. G., Cross, R. T., Johnson, E. & Monto, A. S. Influenza Hemagglutination-Inhibition Antibody Titer as a Correlate of Vaccine-Induced Protection. *J Infect Dis* **204**, 1879–1885 (2011).
62. Pedersen, J. C. Hemagglutination-inhibition assay for influenza virus subtype identification and the detection and quantitation of serum antibodies to influenza virus. *Methods in Molecular Biology* **1161**, 11–25 (2014).
63. Lu, S., Lin, S., Zhang, H., Liang, L. & Shen, S. Methods of Respiratory Virus Detection: Advances towards Point-of-Care for Early Intervention. *Micromachines 2021, Vol. 12, Page 697* **12**, 697 (2021).
64. Vemula, S. V. *et al.* Current Approaches for Diagnosis of Influenza Virus Infections in Humans. *Viruses 2016, Vol. 8, Page 96* **8**, 96 (2016).
65. Juarez, D., Long, K. C., Aguilar, P., Kochel, T. J. & Halsey, E. S. Assessment of plaque assay methods for alphaviruses. *J Virol Methods* **187**, 185–189 (2013).
66. Tobita, K., Sugiura, A., Enomoto, C. & Furuyama, M. Plaque assay and primary isolation of influenza a viruses in an established line of canine kidney cells (MDCK) in the presence of trypsin. *Med Microbiol Immunol* **162**, 9–14 (1975).
67. Gaush, C. R. & Smith, T. F. Replication and plaque assay of influenza virus in an established line of canine kidney cells. *Appl Microbiol* **16**, 588–594 (1968).
68. Lin, Y. *et al.* Optimisation of a micro-neutralisation assay and its application in antigenic characterisation of influenza viruses. *Influenza Other Respir Viruses* **9**, 331–340 (2015).
69. Hatakeyama, S. *et al.* Enhanced expression of an α2,6-linked sialic acid on MDCK cells improves isolation of human influenza viruses and evaluation of their sensitivity to a neuraminidase inhibitor. *J Clin Microbiol* **43**, 4139–4146 (2005).
70. Hollý, J. *et al.* Comparison of infectious influenza A virus quantification methods employing immuno-staining. *J Virol Methods* **247**, 107–113 (2017).
71. Karakus, U., Crameri, M., Lanz, C. & Yángüez, E. Propagation and Titration of Influenza Viruses. *Methods in Molecular Biology* **1836**, 59–88 (2018).
72. Klimov, A. *et al.* Influenza virus titration, antigenic characterization, and serological Mmethods for antibody detection. *Methods in Molecular Biology* **865**, 25–51 (2012).
73. Baer, A. & Kehn-Hall, K. Viral Concentration Determination Through Plaque Assays: Using Traditional and Novel Overlay Systems. *JoVE (Journal of Visualized Experiments)* e52065 (2014) doi:10.3791/52065.

74. Stokes, C. E., Bernstein, J. M., Kyger, S. A. & Hayden, F. G. Rapid diagnosis of influenza A and B by 24-h fluorescent focus assays. *J Clin Microbiol* **26**, 1263–1266 (1988).
75. Tobita, K., Sugiura, A., Enomoto, C. & Furuyama, M. Plaque assay and primary isolation of influenza a viruses in an established line of canine kidney cells (MDCK) in the presence of trypsin. *Med Microbiol Immunol* **162**, 9–14 (1975).
76. Tilmanis, D., van Baalen, C., Oh, D. Y., Rossignol, J. F. & Hurt, A. C. The susceptibility of circulating human influenza viruses to tizoxanide, the active metabolite of nitazoxanide. *Antiviral Res* **147**, 142–148 (2017).
77. Stone, E. T., Hirsch, A. J., Smith, J. L., Brien, J. D. & Pinto, A. K. Titration and neutralizing antibody quantification by focus forming assay for Powassan virus. *STAR Protoc* **3**, 101473 (2022).
78. Cresta, D. *et al.* Time to revisit the endpoint dilution assay and to replace the TCID50 as a measure of a virus sample's infection concentration. *PLoS Comput Biol* **17**, e1009480 (2021).
79. Marr, L. C., Tang, J. W., Van Mullekom, J. & Lakdawala, S. S. Mechanistic insights into the effect of humidity on airborne influenza virus survival, transmission and incidence. *J R Soc Interface* **16**, (2019).
80. Leung, N. H. L. & Milton, D. K. New WHO proposed terminology for respiratory pathogen transmission. *Nature Reviews Microbiology 2024 22:8* **22**, 453–454 (2024).
81. Global technical consultation report on proposed terminology for pathogens that transmit through the air. Retrieved 15 August 2025 from https://www.who.int/publications/m/item/global-technical-consultation-report-on-proposed-terminology-for-pathogens-that-transmit-through-the-air.
82. Andersen, A. A. New Sampler For The Collection, Sizing, And Enumeration Of Viable Airborne Particles,. *J Bacteriol* **76**, 471 (1958).
83. May, K. R. & Harper, G. J. The Efficiency of Various Liquid Impinger Samplers in Bacterial Aerosols. *Br J Ind Med* **14**, 287 (1957).
84. Jang, J., Akin, D. & Bashir, R. Effects of inlet/outlet configurations on the electrostatic capture of airborne nanoparticles and viruses. *Meas Sci Technol* **19**, 065204 (2008).
85. Pan, M. *et al.* Efficient collection of viable virus aerosol through laminar-flow, water-based condensational particle growth. *J Appl Microbiol* **120**, 805–815 (2016).
86. Lindsley, W. G., Schmechel, D. & Chen, B. T. A two-stage cyclone using microcentrifuge tubes for personal bioaerosol sampling. *Journal of Environmental Monitoring* **8**, 1136–1142 (2006).
87. McDevitt, J. J. *et al.* Development and Performance Evaluation of an Exhaled-Breath Bioaerosol Collector for Influenza Virus. *Aerosol Science and Technology* **47**, 444–451 (2013).
88. Pan, M., Lednicky, J. A. & Wu, C. Y. Collection, particle sizing and detection of airborne viruses. *J Appl Microbiol* **127**, 1596–1611 (2019).
89. Lednicky, J. A. *et al.* Viable SARS-CoV-2 in the air of a hospital room with COVID-19 patients. *International Journal of Infectious Diseases* **100**, 476–482 (2020).

90. Pan, M. *et al.* Collection of airborne bacteria and yeast through water-based condensational growth. *Aerobiologia (Bologna)* **34**, 337–348 (2018).
91. Lednicky, J. *et al.* Highly efficient collection of infectious pandemic influenza H1N1 virus (2009) through laminar-flow water based condensation. *Aerosol Science and Technology* **50**, i–iv (2016).
92. Li, H. *et al.* Environmental Surveillance and Transmission Risk Assessments for SARS-CoV-2 in a Fitness Center. *Aerosol Air Qual Res* **21**, (2021).
93. Lednicky, J. A. *et al.* Viable SARS-CoV-2 in the air of a hospital room with COVID-19 patients. *International Journal of Infectious Diseases* **100**, 476–482 (2020).
94. Vass, W. B. *et al.* Viable SARS-CoV-2 Delta variant detected in aerosols in a residential setting with a self-isolating college student with COVID-19. *J Aerosol Sci* **165**, 106038 (2022).
95. Chen, Y. *et al.* The BioCascade impactor: A novel device for direct collection of size-fractionated bioaerosols into liquid medium. *Aerosol Science and Technology* **58**, 264–275 (2024).
96. Nannu Shankar, S. *et al.* The BioCascade-VIVAS system for collection and delivery of virus-laden size-fractionated airborne particles. *J Aerosol Sci* **175**, 106263 (2024).
97. Eiguren Fernandez, A., Lewis, G. S. & Hering, S. V. Design and Laboratory Evaluation of a Sequential Spot Sampler for Time-Resolved Measurement of Airborne Particle Composition. *Aerosol Sci Technol* **48**, 655 (2014).
98. Zervaki, O., Stump, B., Keady, P., Dionysiou, D. D. & Kulkarni, P. NanoSpot™ collector for aerosol sample collection for direct microscopy and spectroscopy analysis. *Aerosol Sci Technol* **57**, 342 (2023).
99. Zhu, P. & Wang, L. Passive and active droplet generation with microfluidics: a review. *Lab Chip* **17**, 34–75 (2016).
100. Chong, Z. Z. *et al.* Active droplet generation in microfluidics. *Lab Chip* **16**, 35–58 (2015).
101. Thorsen, T., Roberts, R. W., Arnold, F. H. & Quake, S. R. Dynamic pattern formation in a vesicle-generating microfluidic device. *Phys Rev Lett* **86**, 4163–4166 (2001).
102. Gañán-Calvo, A. M. Generation of Steady Liquid Microthreads and Micron-Sized Monodisperse Sprays in Gas Streams. *Phys Rev Lett* **80**, 285 (1998).
103. Huang, S. H., Tan, W. H., Tseng, F. G. & Takeuchi, S. A monolithically three-dimensional flow-focusing device for formation of single/double emulsions in closed/open microfluidic systems. *Journal of Micromechanics and Microengineering* **16**, 2336 (2006).
104. Takeuchi, S., Garstecki, P., Weibel, D. B. & Whitesides, G. M. An axisymmetric flow-focusing microfluidic device. *Advanced Materials* **17**, 1067–1072 (2005).
105. Lee, W., Walker, L. M. & Anna, S. L. Role of geometry and fluid properties in droplet and thread formation processes in planar flow focusing. *Physics of Fluids* **21**, (2009).
106. Anna, S. L., Bontoux, N. & Stone, H. A. Formation of dispersions using "flow focusing" in microchannels. *Appl Phys Lett* **82**, 364–366 (2003).

107. Kiss, M. M. *et al.* High-throughput quantitative polymerase chain reaction in picoliter droplets. *Anal Chem* **80**, 8975–8981 (2008).
108. Ahrberg, C. D., Lee, J. M. & Chung, B. G. Microwell Array-based Digital PCR for Influenza Virus Detection. *Biochip J* **13**, 269–276 (2019).
109. Kreutz, J. E. *et al.* Theoretical design and analysis of multivolume digital assays with wide dynamic range validated experimentally with microfluidic digital PCR. *Anal Chem* **83**, 8158–8168 (2011).
110. Zhu, Q. *et al.* Self-priming compartmentalization digital LAMP for point-of-care. *Lab Chip* **12**, 4755–4763 (2012).
111. Hu, Y., Xu, P., Luo, J., He, H. & Du, W. Absolute Quantification of H5-Subtype Avian Influenza Viruses Using Droplet Digital Loop-Mediated Isothermal Amplification. *Anal Chem* **89**, 745–750 (2017).
112. Lindström, S., Mori, K., Ohashi, T. & Andersson-Svahn, H. A microwell array device with integrated microfluidic components for enhanced single-cell analysis. *Electrophoresis* **30**, 4166–4171 (2009).
113. Amselem, G., Guermonprez, C., Drogue, B., Michelin, S. & Baroud, C. N. Universal microfluidic platform for bioassays in anchored droplets. *Lab Chip* **16**, 4200–4211 (2016).
114. Padmanabhan, S. *et al.* Sample filling, discretization, and loop-mediated isothermal amplification in disposable thermoplastic 2D microwell arrays. *Biomicrofluidics* **14**, 014113 (2020).
115. Padmanabhan, S. *et al.* Reagent integration and controlled release for multiplexed nucleic acid testing in disposable thermoplastic 2D microwell arrays. *Biomicrofluidics* **15**, 014103 (2021).
116. Bohl, B., Steger, R., Zengerle, R. & Koltay, P. Multi-layer SU-8 lift-off technology for microfluidic devices. *Journal of Micromechanics and Microengineering* **15**, 1125 (2005).
117. Wu, Z. & Hjort, K. Surface modification of PDMS by gradient-induced migration of embedded Pluronic. *Lab Chip* **9**, 1500–1503 (2009).
118. Takada, K. *et al.* A humanized MDCK cell line for the efficient isolation and propagation of human influenza viruses. *Nat Microbiol* **4**, 1268–1273 (2019).
119. Shu, B. *et al.* Multiplex Real-Time Reverse Transcription PCR for Influenza A Virus, Influenza B Virus, and Severe Acute Respiratory Syndrome Coronavirus 2. *Emerg Infect Dis* **27**, 1821–1830 (2021).
120. Xia, Y. & Whitesides, G. M. Soft Lithography. *Annual Review of Materials Science* **28**, 153–184 (1998).
121. Bordenave, L., Bareille, R., Lefebvre, F., Caix, J. & Baquey, C. H. Cytocompatibility study of NHLBI primary reference materials using human endothelial cells. *J Biomater Sci Polym Ed* **3**, 509–516 (1992).
122. Park, J. H., Park, K. D. & Bae, Y. H. PDMS-based polyurethanes with MPEG grafts: synthesis, characterization and platelet adhesion study. *Biomaterials* **20**, 943–953 (1999).
123. Lee, J. N., Jiang, X., Ryan, D. & Whitesides, G. M. Compatibility of Mammalian Cells on Surfaces of Poly(dimethylsiloxane). (2004) doi:10.1021/LA048562.
124. Piruska, A. *et al.* The autofluorescence of plastic materials and chips measured under laser irradiation. *Lab Chip* **5**, 1348–1354 (2005).

125. Wong, I. & Ho, C. M. Surface molecular property modifications for poly(dimethylsiloxane) (PDMS) based microfluidic devices. *Microfluidics and Nanofluidics 2009 7:3* **7**, 291–306 (2009).
126. Halldorsson, S., Lucumi, E., Gómez-Sjöberg, R. & Fleming, R. M. T. Advantages and challenges of microfluidic cell culture in polydimethylsiloxane devices. *Biosens Bioelectron* **63**, 218–231 (2015).
127. Au, S. H., Kumar, P. & Wheeler, A. R. A new angle on Pluronic additives: Advancing droplets and understanding in digital microfluidics. *Langmuir* **27**, 8586–8594 (2011).
128. Basu, A. S. Digital Assays Part I: Partitioning Statistics and Digital PCR. *SLAS Technol* **22**, 369–386 (2017).
129. Dube, S., Qin, J. & Ramakrishnan, R. Mathematical Analysis of Copy Number Variation in a DNA Sample Using Digital PCR on a Nanofluidic Device. *PLoS One* **3**, e2876 (2008).
130. Bernasconi, C., Katugampola, L. & Wildum, S. Comparison of influenza viral load in nasopharyngeal and midturbinate swabs. *Influenza Other Respir Viruses* **18**, e13253 (2024).
131. Taylor, P. Ostwald ripening in emulsions. *Adv Colloid Interface Sci* **75**, 107–163 (1998).
132. Song, M. G., Jho, S. H., Kim, J. Y. & Kim, J. D. Rapid Evaluation of Water-in-Oil (w/o) Emulsion Stability by Turbidity Ratio Measurements. *J Colloid Interface Sci* **230**, 213–215 (2000).
133. Agarkhed, M. *et al.* Effect of Polysorbate 80 Concentration on Thermal and Photostability of a Monoclonal Antibody. *AAPS PharmSciTech* **14**, 1 (2012).
134. Bousse, T. *et al.* Quantitation of influenza virus using field flow fractionation and multi-angle light scattering for quantifying influenza A particles. *J Virol Methods* **193**, 589 (2013).
135. Fusion Series User Manual. Retrieved 15 August 2025 from https://www.chemyx.com/downloads/fusion-series-manual.pdf
136. Mashiyama, S. *et al.* Pushing the limits of microfluidic droplet production efficiency: engineering microchannels with seamlessly implemented 3D inverse colloidal crystals. *Lab Chip* **24**, 171–181 (2024).

List of Publications and Conference Presentations

Publications that have appeared in print:

1. Srimathi, Siddharth Raghu, et al. "Microfluidic digital focus assays for the quantification of infectious influenza virus." *Lab on a Chip* 25.8 (2025): 2004-2016.

Presentations that have been delivered:

1. *Microfluidic Digital Focus Assay for the Quantification of Infectious Influenza Virus (poster)*
   Siddharth Raghu Srimathi, Maxinne A. Ignacio, Maria Rife, Sheldon Tai, Donald K. Milton, Margaret A. Scull, Don L. DeVoe
   The 28th International Conference on Miniaturized Systems for Chemistry and Life Sciences (μTAS 2024), Montreal, Canada, Oct 2024
2. A Digital Focus Forming Assay Platform for the Quantification of Infectious Influenza Virus
   Siddharth Raghu Srimathi, Maxinne A. Ignacio, Margaret A. Scull, Don L. DeVoe
   2023 AIChE Annual Meeting, Orlando, FL, Nov 2023
3. Digital focus assay platform for the quantification of viable viruses (poster)
   Siddharth Raghu Srimathi, Maxinne A. Ignacio, Margaret A. Scull, and Don L. DeVoe
   The 27th International Conference on Miniaturized Systems for Chemistry and Life Sciences (MicroTAS 2022), Katowice, Poland, October 2023
4. A digital culture platform for studying virus distribution in respiratory aerosols (poster)
   Siddharth Raghu Srimathi and Don L. DeVoe
   The 26th International Conference on Miniaturized Systems for Chemistry and Life Sciences (MicroTAS 2022), Hangzhou, China, October 2022